Characterization of 3D-Printed Superconducting Arches with Electron-beam Induced Deposition using a Computer Aided Design Program

THESIS

submitted in partial fulfillment of the
requirements for the degree of

MASTER OF SCIENCE
in
PHYSICS

Author :	V.A. Wagemans
Student ID :	s1532413
Supervisor :	Prof.dr. J. Aarts & Dr. K. Lahabi
2nd corrector :	Prof.dr. J.M. van Ruitenbeek

Leiden, The Netherlands, May 25, 2021

Characterization of 3D-Printed Superconducting Arches with Electron-beam Induced Deposition using a Computer Aided Design Program

V.A. Wagemans

Huygens-Kamerlingh Onnes Laboratory, Leiden University
P.O. Box 9500, 2300 RA Leiden, The Netherlands

May 25, 2021

Abstract

Focused electron-beam induced deposition (FEBID) is a non-destructive, relatively fast and cheap method with applications in AFM, plasmonics and nanomagnetics amongst others. In this thesis, three dimensional superconducting arches were fabricated using this technique with the help of a computer aided design (CAD) program. Magnetic field sweeps were performed at low temperatures ($\sim$ 2-5 K) to characterize these arches. With a few improvements, more complex 3D structures can be fabricated, paving the way towards the numerous applications people now can only dream of.

Contents

1 Introduction **1**

2 Theory & EBID parameters **3**
2.1 Superconductivity . . . 3
2.2 Simple Deposition Growth Model . . . 4
2.3 EBID parameters . . . 5
2.3.1 Electron-beam parameters . . . 5
2.3.2 Scanning pattern and strategy . . . 9
2.3.3 Beam-induced heating . . . 12

3 CAD program **13**
3.1 Introduction . . . 13
3.2 Calibration files . . . 14
3.3 Vertical growth rate . . . 16
3.4 Pixel point pitch and exposure pattern pixel size . . . 18
3.5 Designs . . . 19
3.6 Hybrid Monte-Carlo simulation . . . 21

4 Transport Measurements of EBID nanostructures **23**
4.1 Resistance curves & critical temperature . . . 23
4.1.1 Calculation of Ginzburg-Landau parameter . . . 25
4.2 Current characteristics . . . 26

5 Conclusion & Outlook **29**
5.1 Conclusion . . . 29
5.2 Outlook . . . 30

Appendix A **31**
A.1 Pillar height dependency . . . 31
A.2 EDX measurement . . . 32

Acknowledgements **33**

Bibliography **35**

CHAPTER 1

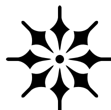

INTRODUCTION

The manufacturing of a superconducting quantum interference device (SQUID) consists of multiple, time-consuming processes, such as sputtering deposition, lithography, focused ion-beam milling and (ion-beam) etching[1,2]. Hence, researching a faster and cheaper way of making such devices, while maintaining quality of course, is of great importance. One way to make this possible is by using the technique called focused electron-beam induced deposition (FEBID). This allows for a creation of SQUIDs at submicrometer scale, within a much shorter period of time and without the need of multiple expensive pieces of equipment. Other applications for this method are in AFM[3], plasmonics[4] and nanomagnetics[5–8]. EBID can also be used in applications to make nano-electromechanical systems (NEMS)[9], gas sensors[10] or biosensors[11,12].
In this project the focus will be on making 3D structures like arches, and on the use of the computer aided design (CAD) program from Ref. 13.

A scanning electron microscope (SEM) is used in conjunction with an implemented gas injection system (GIS) to fabricate nano structures with EBID. Figure 1.1 shows how it works. First (left picture) gas molecules flow onto the substrate using the GIS. These precursor molecules then adhere onto the substrate. An electron beam from the SEM dissociates the precursor molecules (middle); in the case of tungsten hexacarbonyl, $W(CO)_6$, the tungsten and carbon group are separated. Fully dissociation happens when six electrons with enough energy to break the molecular bonds, interact with the molecule, leaving the tungsten to attach to the substrate and the volatile carbon group to escape that same substrate.
If this process is repeated long enough, the tungsten will form a structure that depends on the settings of the beam, i.e. the beam current, dwell time and pitch (right picture). The dwell time is a measure of the time the beam stays at one spot. The pitch corresponds to the distance the e-beam travels per time step. When the beam does not move, the tungsten will be deposited on top of each other, thus forming a straight pillar. A segment is formed when the beam travels some distance, and is defined as part of a structure that has a non-right angle w.r.t. the substrate. Essentially, if it is not a pillar, it is a segment. In the right picture of figure 1.1 a segment is shown.

The CAD program works only when the right input is given. For that, one needs to implement two calibration files. One is a list of segment angles as a function of dwell time, and the other is a list of settings. After the input is submitted, positions and dwell times are calculated accordingly to form streamfiles that are used by the SEM for deposition. More on this topic is found in chapter 3.

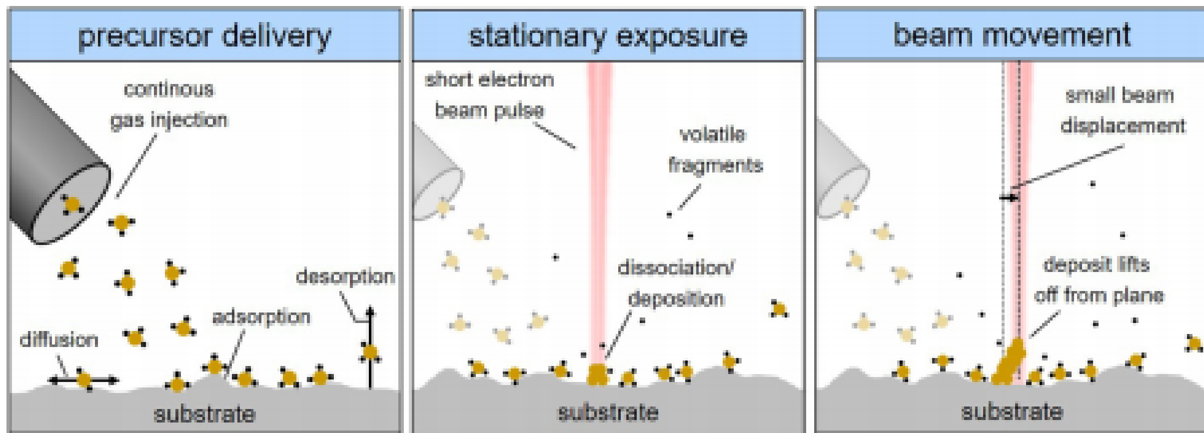

Figure 1.1: *Schematic representation of the (F)EBID process. There is a flux of incoming precursor molecules via the GIS (left). An electron beam dissociates the precursor gas, allowing for growth of nanostructures. A pillar is formed when not moving the beam (middle). When the beam travels at a slow enough speed, a segment is formed (right). Taken from Ref. 14.*

Chapter 2 on the other hand, gives an introduction into EBID theory (section 2.2). A discussion about the influence of different parameters is presented afterwards, in section 2.3. As stated above, chapter 3 gives more information about the calibration files (section 3.2), as well as results from experiments done using streamfiles made with the CAD program (section 3.3-3.5). Measurement results can be found in chapter 4, as is the set-up used for measuring (section 4.1). Finally, a conclusion is given in chapter 5, together with a look into future developments.

CHAPTER 2

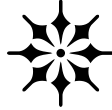

THEORY & EBID PARAMETERS

This chapter is an introductory chapter to some relevant theory, as well as a more rigorous overview of the parameters used in EBID, together with the dependency of the deposition growth on those parameters.

2.1 Superconductivity

Superconductivity is a phenomenon where the electrical resistance of a material drops to zero when lowered to below a certain critical temperature (T_c), as shown in figure 2.1. Its theoretical explanation comes from quantum mechanics, even though it is a macroscopic phenomenon. Below the critical temperature, the electrons in the material form pairs, so-called Cooper pairs. Pairs of electrons have an even spin number, either spin 0 or spin 1, and thus they are bosons, whereas single electrons are fermions, with spin 1/2. So by forming pairs, the Pauli exclusion principle does not apply anymore, and the Cooper pairs form a bosonic condensate, occupying only the lowest energy state. This allows then for the whole macroscopic system to be described by a single wave function. In such a system there is no flow of electrons, but the electrons are connected to every other electron, and thus zero resistance is reached when applying a current.

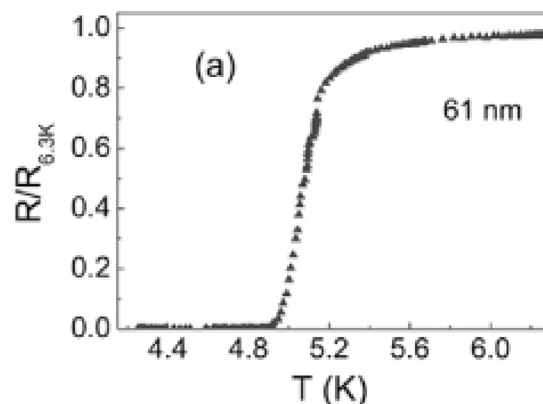

Figure 2.1: *Temperature versus normalized resistance of a tungsten nanowire (61 nm width). A superconducting transition is observed around 5 K. Taken from Ref. 15.*

2.2 Simple Deposition Growth Model

In this section, a simple growth model is presented, taken from Ref. 16. Its starting point is the precursor coverage, N, which is influenced by a few processes. The number of precursor molecules that are adsorbed from the gas phase and stick unto the substrate (first term), the number of molecules that are decomposed by the e-beam (second term), and the number of molecules that desorb to the gas phase, being released by the substrate (last term).

$$\frac{dN}{dt} = gF\left(1 - \frac{N}{N_0}\right) - \sigma(E)NJ - \frac{N}{\tau} \tag{2.1}$$

Here, g is the sticking factor, F is the influx of precursor molecules on the substrate, N_0 is the available adsorption site density for a mono-layer, σ(E) is the cross-section of precursor dissociation, J is the current density and τ is the residence time. Two simplifications are made, concerning the cross-section and the current density. The cross-section as a function of energy, σ, is not known and therefore the integrated value, σ, is used. The current density is the sum of all contributions from primary electrons (PE), secondary electrons (SE) and back-scattered electrons (BSE). However, SE's and BSE's are not measured during experiments and as such, it is assumed that $J = J_{PE}$. When the precursor molecule coverage is constant we get the following steady-state solution:

$$N = N_0 \left[\frac{\frac{gF}{N_0}}{\frac{gF}{N_0} + \sigma J + \frac{1}{\tau}} \right] \tag{2.2}$$

We can now define the growth rate, R, to be $R = V_{molecule}N\sigma J$, where $V_{molecule}$ is the volume of a single precursor molecule. Remember from equation 2.1 that $N\sigma J$ is the number of molecules per second that are decomposed by the e-beam. Defining the growth rate in this way then makes sense. Combining this definition with equation 2.2 we get an expression for the growth rate.

$$R = V_{molecule}N_0 \frac{\left(\frac{gF}{N_0}\right)\sigma J}{\left(\frac{gF}{N_0} + \sigma J + \frac{1}{\tau}\right)} \tag{2.3}$$

When desorption is ignored one can distinguish two different regimes:

$$\frac{gF}{N_0} \gg \sigma J, \qquad R = V_{molecule}N_0\sigma J, \qquad electron - limited \tag{2.4a}$$

$$\frac{gF}{N_0} \ll \sigma J, \qquad R = V_{molecule}gF, \qquad precursor - limited \tag{2.4b}$$

The first regime depends on the current density, and thus on the beam current. It is independent of the gas flux of precursor molecules. It is therefore called the electron-limited (e.l.) regime. The second regime, however, is only dependent on the incoming precursor molecules and is independent of the parameters for the electron beam. Hence, the precursor-limited (p.l.) regime. Reports of measurements on the growth of nanostructures use different units. Below are two of those units and its relation to the growth rate, R, from the simple model above.

$$V_{deposit} = Rt_{dwell}A_{deposit} \tag{2.5a}$$

$$h_{deposit} = Rt_{dwell} \tag{2.5b}$$

Here, $V_{deposit}$, $A_{deposit}$ and $h_{deposit}$ are the deposited volume, area and height respectively. A new, important parameter is the dwell time, t_{dwell}. This is the time the e-beam stays on the same spot. The longer it stays at a certain spot, the more growth one gets. From Monte Carlo simulations done by Fowlkes *et al.*[17], it showed that vertical growth is mostly due to PE's. Thus, when defining the growth efficiency to be the height per PE, we get the highest growth efficiency in the e.l. regime.

An example where desorption cannot be ignored is when the temperature is varied. Thus the above simplifications cannot be made. However, there is a relation between the residence time, τ, and the temperature.

$$\tau = \frac{1}{\nu} e^{E_{des}/k_B T} \tag{2.6}$$

Here, ν is the vibrational frequency of an adsorbed molecule, E_{des} the desorption energy and k_B the Boltzmann constant. When the temperature increases, the residence time will decrease, and from equation 2.3 we can see that then also the growth rate R decreases.

From Ref. 16, Sec. IV, we can see that the simple growth model explains experiments qualitatively very well. A few parameters from this model, like the beam current and the dwell time, are discussed experimentally in the next section. Other important parameters, such as electron energy and scanning speed, are also added to the discussion.

2.3 EBID parameters

This section discusses the influence of certain parameters on the growth of nanostructures. Subsection 2.3.1 deals with the properties of the electron beam, whereas subsection 2.3.2 deals with the scanning pattern and strategy, thus including the pitch and dwell time. Finally, a short subsection is dedicated to the effect of beam-induced heating.

2.3.1 Electron-beam parameters

The influence of the beam current on the height of a deposition is simple to explain. If the current becomes higher, more electrons are injected into the system, increasing the chance of dissociation of precursor molecules. This leads to more growth, and, as previously stated, vertical growth is dominated by the primary electrons[17], i.e. the e-beam current. Thus with increasing beam current, more vertical growth is expected. Looking back at section 2.2, linear behaviour is expected in the electron-limited regime, whereas in the precursor-limited regime the growth is independent of the beam current. A transition from e.l. to p.l. should therefore show a saturation in a beam current versus depositon growth plot. Below is an example of this, shown in figure 2.2. For tetra-ethoxy-silane (squares) between 20 and 100 pA, a saturation is seen, indeed indicating a transition from e.l. to p.l. regime. This transition is much more obvious for dimethyl acetylacetonate gold (circles), comparing the growth from 200 pA to 6 nA to the growth below 200 pA. The behaviour for contamination growth (triangles) cannot be explained by this simple model. It needs the more complicated model that includes the residence time, τ.

Lateral growth is seen to increase with higher currents as $d_{lat} \sim \sqrt{I}$[18,19]. However, the beam diameter, d_{beam}, also depends on the square root of the current (remember that A_{beam} goes linear with I). The indication that the lateral growth is dependent on d_{beam}, and not on I, is

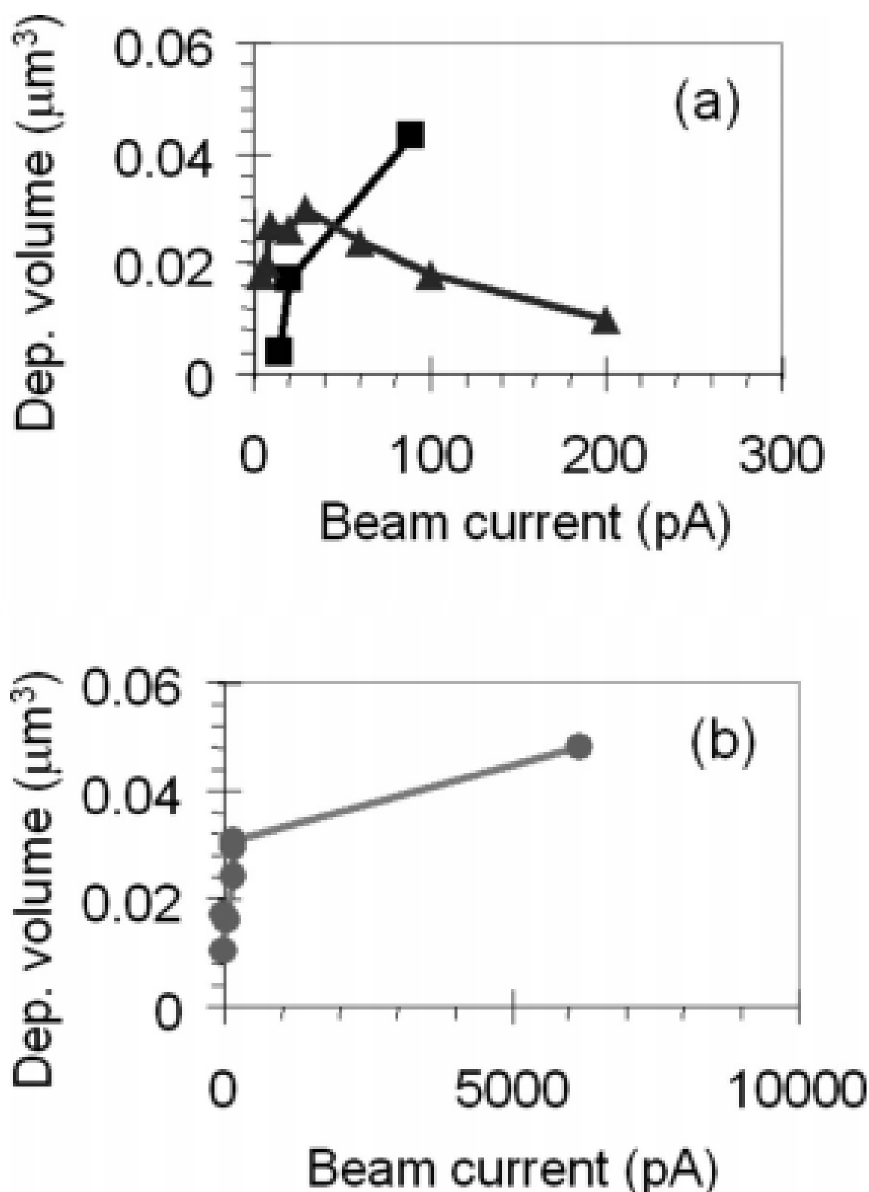

Figure 2.2: *Beam current versus deposition growth for tetra-ethoxy-silane (squares)*[20] *and dimethyl acetylacetonate gold (circles)*[18]*, showing a transition from the e.l. regime to the p.l. regime. The dwell time is 120s for every point in the plots. Taken from Ref. 16*

confirmed by Beaulieu *et al.*[21], who reported lateral growth independent on the current.

The lateral deposition growth also depends on the charge and the dwell time. Figure 2.3 shows experimental results of lateral growth for pillars as a function of dwell time. This fast increase at the beginning and the saturation after a certain time is observed by multiple research groups[19,21–25]. A model was made by Silvis-Cividjian *et al.* to explain this growth behaviour[26]. This model uses only the secondary electrons in its calculation of the cross section, but manages to give a qualitative description of the lateral growth behaviour. However, Fowlkes *et al.*[17], takes also into account the PE's and the BSE's. This study shows that the lateral growth is dominated by the SE's.

Increasing the current leads also to an increase in metallicity. This is due to the fact that more electrons in the system speed up dissociation, and therefore more fully dissociated precursor molecules adhere unto the substrate. These molecules consist often of metals, like tungsten

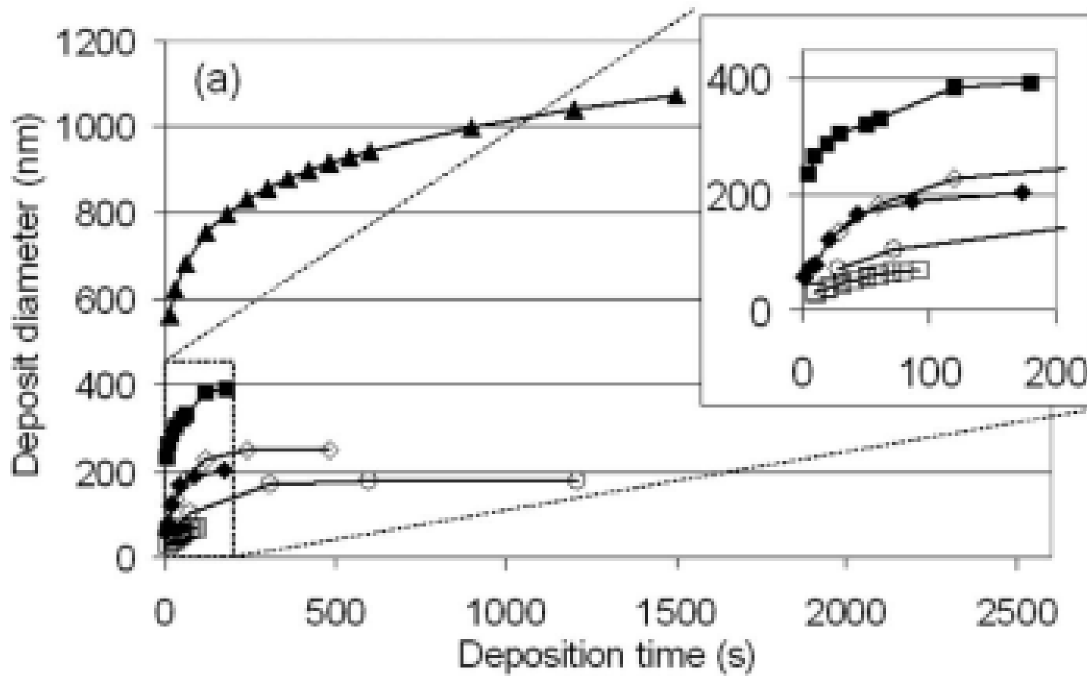

Figure 2.3: *Lateral deposition growth versus dwell time from different experiments*[19–21,23,25,27]. *Taken from Ref. 16.*

hexacarbonyl. Desorption of the volatile component is increased as well. Beam-induced heating can also play a part in the latter (more on this topic in section 2.3.3).
As the metallicity goes up when current increases, the resistivity obviously decreases. An experiment by Ref. 24 showed that at the beginning the resistivity decreases rapidly and non-linear, explained by a change in structure of the conducting wire, and after which the resistivity went down linearly due to an increase in wire cross section.

The height of a structure is also dependent on electron beam energy. The lateral growth, however, depends very little on the electron energy due to a change in beam diameter when the electron energy is changed[19].
Studies show that low-energy (secondary) electrons, up to a few hundred eV, contribute significantly to the growth of deposits[28–33]. These electrons interact via dissociative electron attachment (DEA) and dipolar dissociation (DD)[28]. An important process with electrons that have higher energy is dissociative ionization (DI)[34]. All these processes have their maximum cross section below 1 keV, and as a higher cross section means more growth, it is an argument for keeping the primary electron energy below this threshold. However, the density of (primary) electrons is much higher directly under the electron beam than the density of the low-energy (secondary) electrons. In this way, a beam energy higher than 1 keV can still be useful in stimulating the growth of structures.
Figure 2.4 shows two graphs from experiments that use a large range in energy, up to 30 keV (or kV, which is the same). The graph in 2.4a can be explained using the next figure (2.5), in which the total yield of SE's and BSE's is plotted as a function of primary electron energy. A rapid decrease starting from a few hundred eV to 10 keV and a constant value from there on forward indicates that the main growth was due to SE's. We already know from Ref. 17 that primary electrons are the most dominant source of vertical growth. As a matter of fact, figure 2.5 holds only for flat surfaces. And the situation becomes different and more complicated when actually taking into account a growing structure. Primary electrons with higher energies have a much greater chance at exiting the structure tip. Low-energy

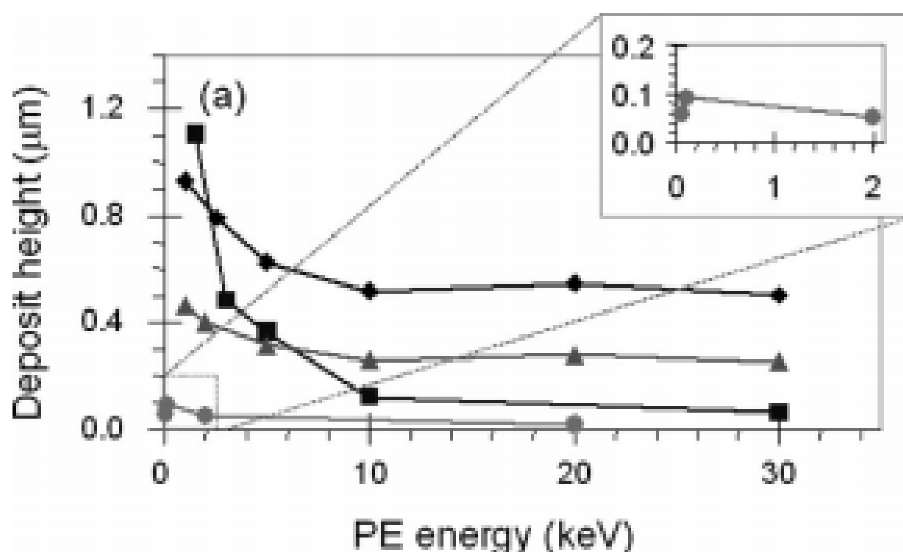

(a)

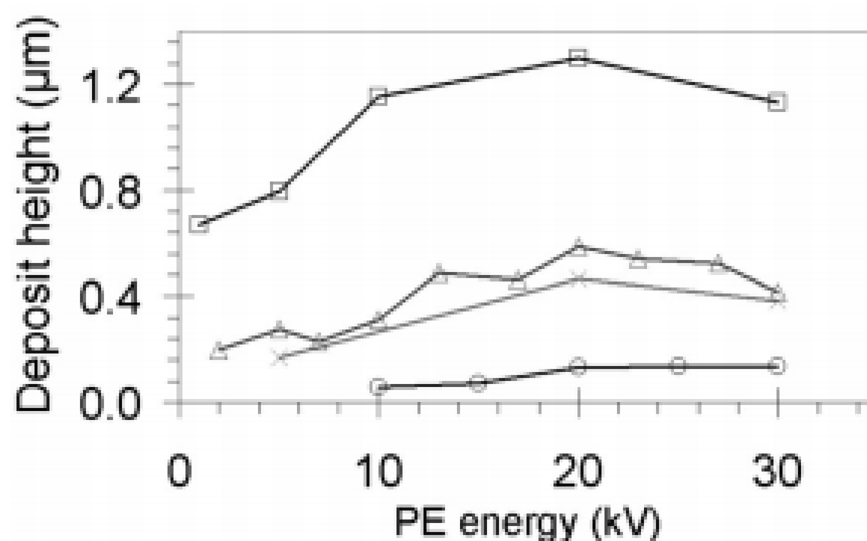

(b)

Figure 2.4: *Deposit height as a function of primary electron energy. Figure (a) shows a dependency corresponding to the generation of SE's and BSE's. Experiments are from Refs. 35–38. Figure (b) shows a different dependency, in line with simulations[17]. These experiments are from Refs. 19,23,39, 40. Taken from Ref. 16.*

electrons interact mostly within the tip, heating it up. This beam-induced heating lowers the residence time of the precursor molecules, and through this effect the vertical growth rate goes down. This would then explain the results found in figure 2.4b.

Conductivity measurements are inconsistent. Hoyle *et al.* found for $W(CO)_6$, the precursor also used in this thesis, that conductivity increases as the electron energy decreases[35]. It was confirmed by experiments from Kohlmann-von Platen *et al.*, using the same precursor molecule[41]. However, another group found the opposite effect with the precursor MeCpPtMe_3[42]. The difference in dependency is yet to be understood.

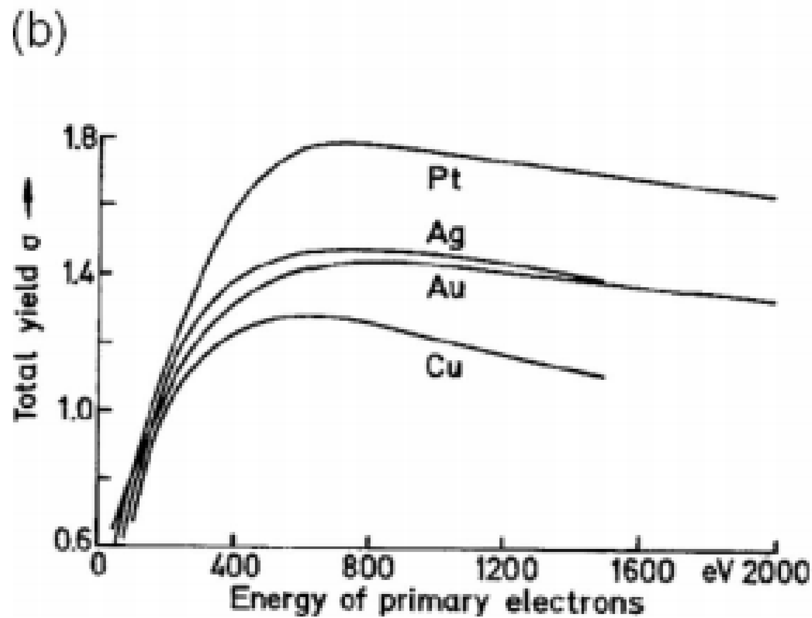

Figure 2.5: *Total yield of electrons (SE's + BSE's) as a function of primary electron energy. Taken from Ref. 43.*

2.3.2 Scanning pattern and strategy

The scanning pattern is the influence of the geometry of the structure one builds, i.e. the presence of a line can influence the height of another structure (a dot or another line) just by being close to it. In the previous discussion we looked at isolated tips (or pillars). This section then gives some insight into non-isolated structures.

The growth process is highly dependent on the regime it is in, e.l. or p.l, which was discussed in section 2.1. In the extreme case that growth is almost immediately in the precursor-limited regime, height differences were seen for contamination growth experiments[44,45] and lines[46]. It is explained by surface diffusion. When in the p.l. regime, the area under the beam will have depleted the supply of precursor molecules fast, and new ones now have to come from outside the irradiated area. With diffusion as the main supply mechanism, the molecules will be pinned before they can reach far inside the irradiated area. In this way, the growth forms a ring with a diameter being the diameter of the electron beam. This is indeed observed in Ref. 44 and Ref. 45. Theoretical models by Utke *et al.*[47] and Smith *et al.*[48] describe the growth behaviour in the two regimes well.

The scanning strategy entails parameters like the dose per scan (amount of charge), dwell time and loop time. These are talked about in the first paragraph. The second paragraph is about the scanning speed. The last two items are the position of the gas nozzle and the pitch (or overlap).

Kohlmann-von Platen *et al.*[41] studied both the effect of a changing dwell time and a changing loop time, while keeping the dose per charge constant, using the precursor $W(CO)_6$. The loop time is simply the time between subsequent visits of the same spot on the substrate. It is usually beneficial for the structure to deposit multiple times on all positions governed by the stream file. When the loop time was held constant, they found for decreasing dwell time an increase in deposition yield. The dissociation rate is much higher at low dwell times than at high dwell times. Thus, when given some time to replenish, i.e. the loop time, a larger

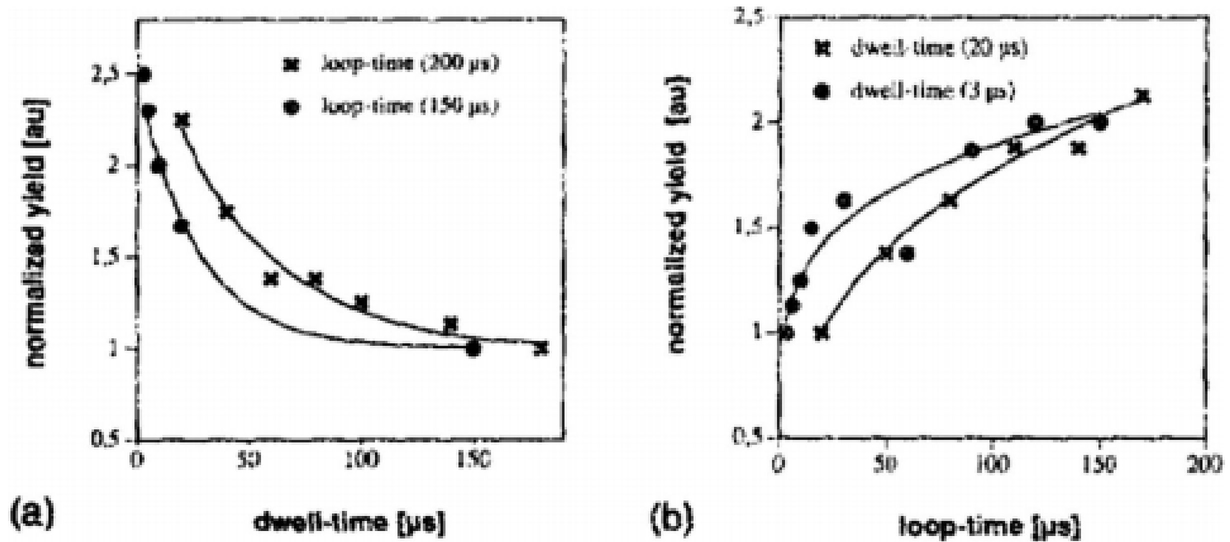

Figure 2.6: *Normalized deposition yield as a function of (a) dwell time and (b) loop time. Taken from Ref. 41.*

yield is obtained in comparison to continuous exposure. A higher loop time means there is more time to replenish the decomposed precursor molecules, giving an even larger yield. This is depicted in the left picture of figure 2.6. The picture on the right side shows the effect of a constant dwell time and a changing loop time. The saturation indicates that the surface coverage N becomes constant at higher loop times and independent of the dwell time.
Other experiments where the loop time was varied confirmed this behaviour[21,46,49]. Saturation, however, occurred at different time scales. This can be explained by a difference in precursor flux for Ref. 46 and a difference in sticking factor of the used precursor for Ref. 49.

The experiments done with a changing dwell time seem to be less consistent. Sanchez *et al.* mentioned a higher growth rate at lower dwell times for deposition of squares, without giving numbers[50]. Lipp *et al.*[49] found a similar effect, but not as pronounced as in Kohlmann-von Platen *et al.*[41]. This might be due to the fact Lipp *et al.* used shorter dwell times than in Ref. 41. However, Beaulieu *et al.* found no significant dependency on dwell time[21]. This then might be explained by the fact Beaulieu *et al.* used much longer dwell times than in the experiments by Kohlmann-von Platen *et al.* and Lipp *et al.*.

Experiments where the dwell time and loop time were varied at the same time, creating a variation in the amount of charge dose per scan, yielded a different resistivity. For fast scans (low dose), with relatively short dwell and loop times, a higher resistivity was found than for slow scans (above 5000 C/m^2)[51]. In the paper they stated that fast scans and slow scans are in two different regimes, electron-flux limited and gas-flux limited respectively. In the last regime, the precursor molecules undergo more collisions with the electrons, leading to an increase in full dissociation. This then leads to a lower resistivity due to the increase in deposited metallic components of the precursor gas. Other experiments, using different precursor gases, confirm this model[52,53].

The scanning speed is another parameter that has influence on deposition. Experiments done by Koops *et al.*[54] and Mølhave *et al.*[55] showed a transition when increasing the scan speed while depositing pillars. Such a transition, from Ref. 56, can be seen in figure 2.7 (a,b). With increasing scan speed the pillar will become more and more inclined. At some point, a

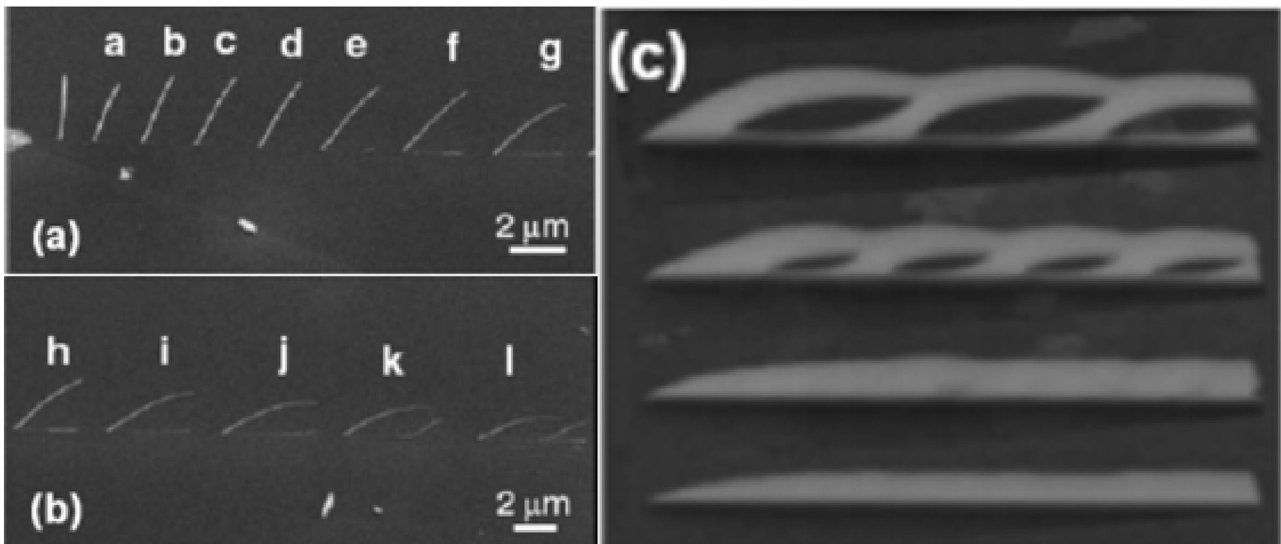

Figure 2.7: *The deposition of pillars while increasing the scanning speed. The higher the speed, the more the pillars are inclined (a). A secondary pillar is also formed due to thinning of the primary structure, which lets electrons easier penetrate (b). At the highest speed primary and secondary pillars meet and form a fencelike structure until a solid line is deposited (c). Taken from Ref. 56 (a,b) and Ref. 57 (c).*

new, second structure is formed as well. Eventually, this second structure will connect to the first one, making a fencelike structure[57]. With even faster scans, a solid line is deposited. This is shown in figure 2.7 (c). The growth of the secondary structures is due to electrons penetrating the first pillar. As the scan speed increases, the first pillar becomes thinner and thinner, and more electrons can penetrate. As stated above, this will then lead to the fence-like structure in figure 2.7 (c) and finally the deposition of a solid line.

The position of the gas nozzle w.r.t. the scanning direction influences the vertical growth rate. An experiment that looked at deposition of lines, connected to the bottom of a tip, while changing the scanning direction, either away or towards the gas nozzle, showed there is more vertical growth when the beam is scanned towards the nozzle[58]. This is explained by an inhomogeneity of the precursor coverage on the tip. The side facing the gas nozzle has a higher precursor coverage than the side opposite the nozzle. Another experiment, where the precursor supply was in stead dominated by surface diffusion, found a similar dependency[59].

The pitch is the last parameter in this section to be discussed. This is simply another word for the step size, which is the change in position of the electron beam after the set dwell time is reached. Decreasing the step size effectively does the same as an increase in dwell time when the step size is smaller than the beam diameter, which has to be the case when writing a continuous structure. The overlapping region will get another dose for the same duration, thus effectively having doubled the dwell time. A different way of describing the above parameter is also used in EBID: the overlap. This is the percentage of the beam surface that overlaps with the beam in the previous step, thus indirectly gives us back the step size (pitch).

If the step size is decreased too much, charging of the structure can occur.

2.3.3 Beam-induced heating

Beam-induced heating, an effect where heat transfers from the PE's to the phonons in the substrate, is subject to great disagreement. Based on calculations, Li and Joy[60] assume that beam-induced heating has a negligible effect on deposition growth. Experiments done by Folch and Servat[61] are in agreement with this conclusion. In contrast, Bret *et al.*[62], Randolph *et al.*[39] and Utke *et al.*[63] assume that the increase in temperature from beam-induced heating is significant, reaching up to 60-80 °C for tip deposition. Looking back at figure 2.2, for contamination (triangles), significant beam-induced heating can explain its behaviour.

Chapter 3

CAD program

This chapter is about the Computer Aided Design (CAD) program from Ref. 13, used to create streamfiles for patterning. A short introduction to the program is given first, followed by preparatory experiments. Also, two distinct designs, made with the CAD program, are presented. In the last section, a feedback mechanism to the program is explained.

3.1 Introduction

For the Computer Aided Design (CAD) program to work, it requires a certain input. This input comes from a few experiments, which will be discussed in detail in the next sections. It entails parameter values that are specific to the set-up you use. A picture of the Graphical User Interface (GUI) is shown in figure 3.1, with in red highlighted regions indicating the important parameters.

Starting from the top right, we have the plot of the segment angle as a function of the dwell

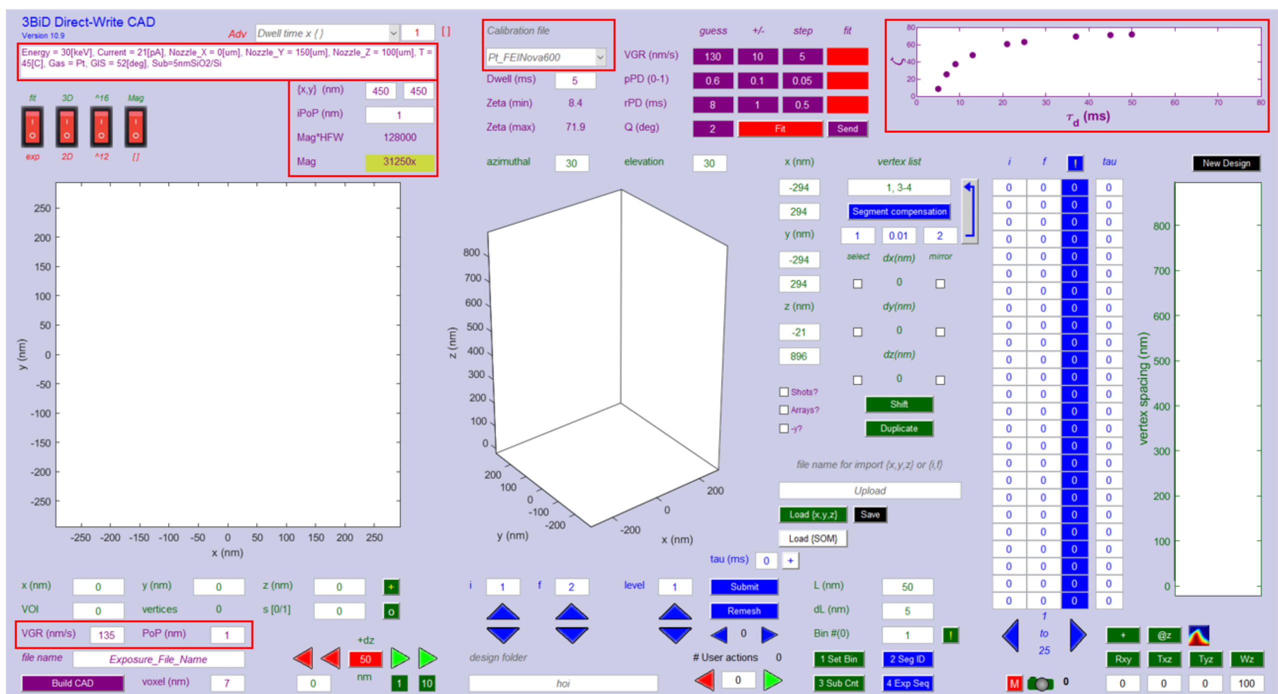

Figure 3.1: *Graphical User Interface (GUI) of the CAD program. Highlighted regions indicate important parameters that are needed to make the program work.*

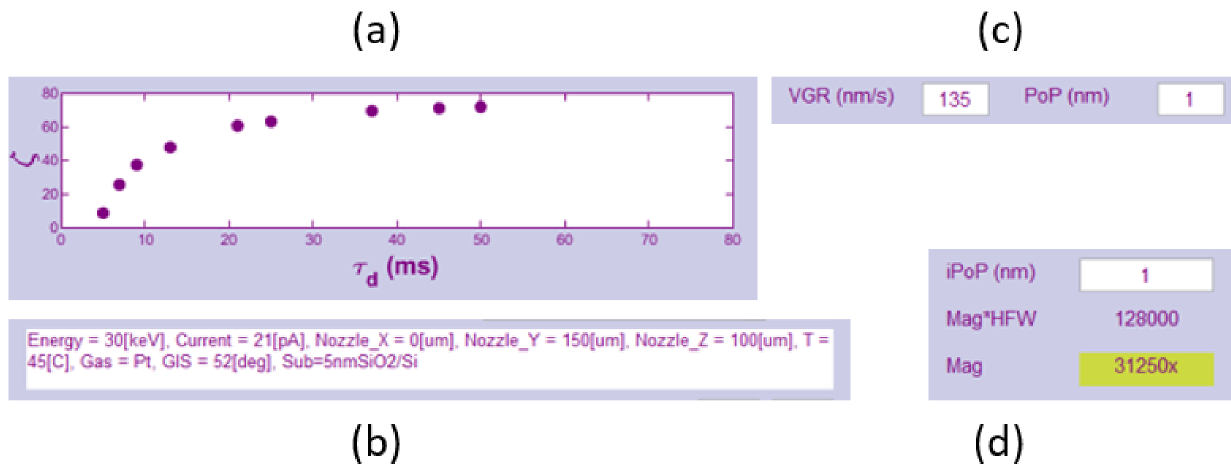

Figure 3.2: *Important parameters for the CAD program, with (a) segment angle as a function of dwell time, (b) parameter file values, (c) vertical growth rate and pixel point pitch, and (d) the exposure pattern pixel size, magnification*(horizontal field width) and the exposure magnification.*

time. When a segment is deposited on top of a pillar, the angle between the horizontal plane, parallel to the substrate, and the segment is dependent on the dwell time used to deposit. This calibration file is accompanied by a file with parameters specific for the SEM used in the experiments. These parameter values are also shown in the program (top left), with one of these shown in a separate box (Mag*HFW). These files both need to be submitted, which is done in the highlighted place in the top middle. For clarity, figure 3.2 shows these parts of the GUI as well.
The second important parameter is the vertical growth rate (VGR), shown at the bottom left. This is used to calculate the total dwell time for a pillar of height L_z.
For segments, the important parameter is the pixel point pitch (PoP), i.e. the beam displacement per exposure. According to Fowlkes *et al.*, values for high resolution segments are in the range of 0.2-2[13]. The exposure pattern pixel size (iPoP) sets the lower limit on this value and is also used in the calculation of the exposure magnification (yellow box).

When all of these parameters are submitted into the program it can calculate the necessary dwell times for the structure. Combining the dwell times and the coordinates, defined by pillars and segments spanning vertices, it creates the corresponding streamfile.
The next three sections deal with all the important parameters and how to get them. After that, designs of a simple and a more complicated arch are presented. The last section gives information about a hybrid Monte-Carlo simulation that can be used as a feedback mechanism.

3.2 Calibration files

Calibration consists of two files; a angle versus dwell time plot and a list of specific parameter values. The latter is the easiest to obtain. These are values that can be looked up for the unique set-up. Only the parameter magnification*HFW needs to be determined by hand. Simply using the line tool to measure up the screen in the horizontal direction does the trick here. Precursor gas type, nozzle (x,y) positions and substrate are just there for your information. The rest is used in the CAD program to create the streamfile. An overview of these parameters used in this project are shown in table 3.1.
To obtain the segment angle versus dwell time plot it is needed to deposit multiple pillars

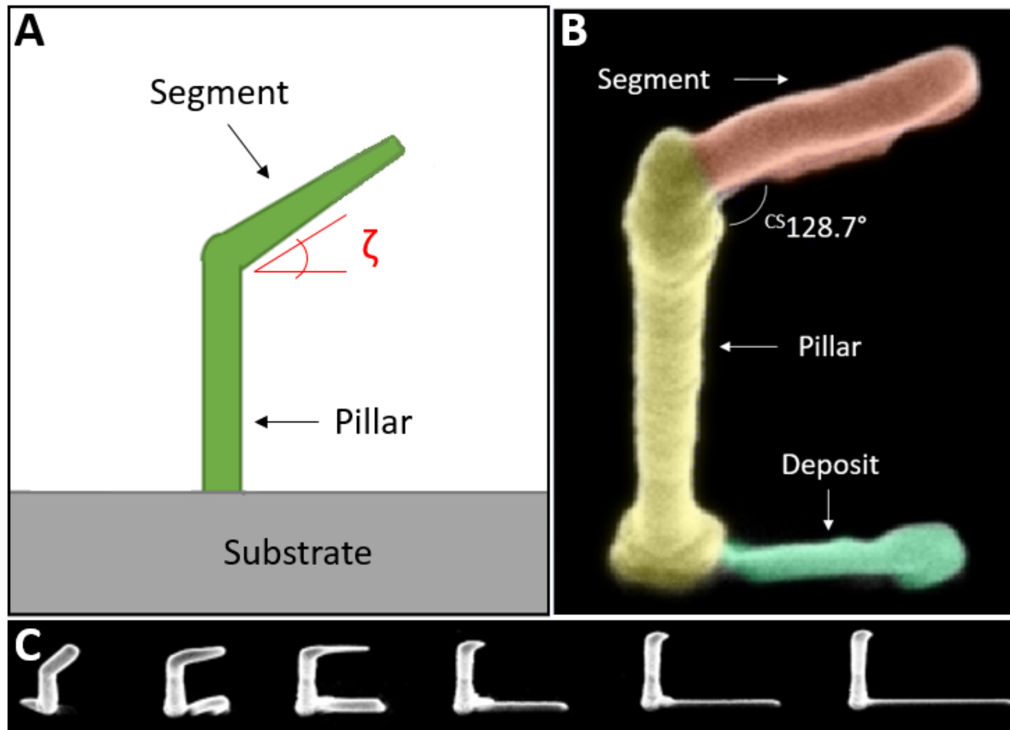

__Figure 3.3:__ (a) Illustration of a pillar and segment deposited with EBID. The angle ζ is measured for multiple segments, all with different dwell times. (b) False-coloured image of a pillar and segment made with the SEM. The angle that is measured is rotated by 90° w.r.t. the angle ζ. (c) Angle as a function of the beam displacement. The step size in between consecutive beam dwells is increased from 0.11 Py to 0.66 Py (1 Py equals 0.31 nm). When the beam displacement gets larger, the growth of the segment lags behind too much for a continuous structure to form. The number of steps and dwell time were held constant.

Table 3.1: *Parameter file for the calibration of the CAD program.*

Parameter	Value
Patterning format	FEI
PE energy [kV]	10
PE current [nA]	5
PE beam size (FWHM) [nm]	17.9
Precursor gas type	W
Precursor temperature [C]	55
Gas nozzle position (x, y, z) [μm]	(0, 150, 150)
Gas nozzle angle [deg]	30
Substrate	SiO_2
(Magnification)*(Horizontal field width [μm])	415.000
Patterning bit depth	16

The beam size value is taken from the SEM in optiplan mode, and thus this mode is also used for deposition of 3D structures (while standard mode was used to obtain the dwell vs angle calibration file). In this mode the beam spot is smaller than in standard mode.

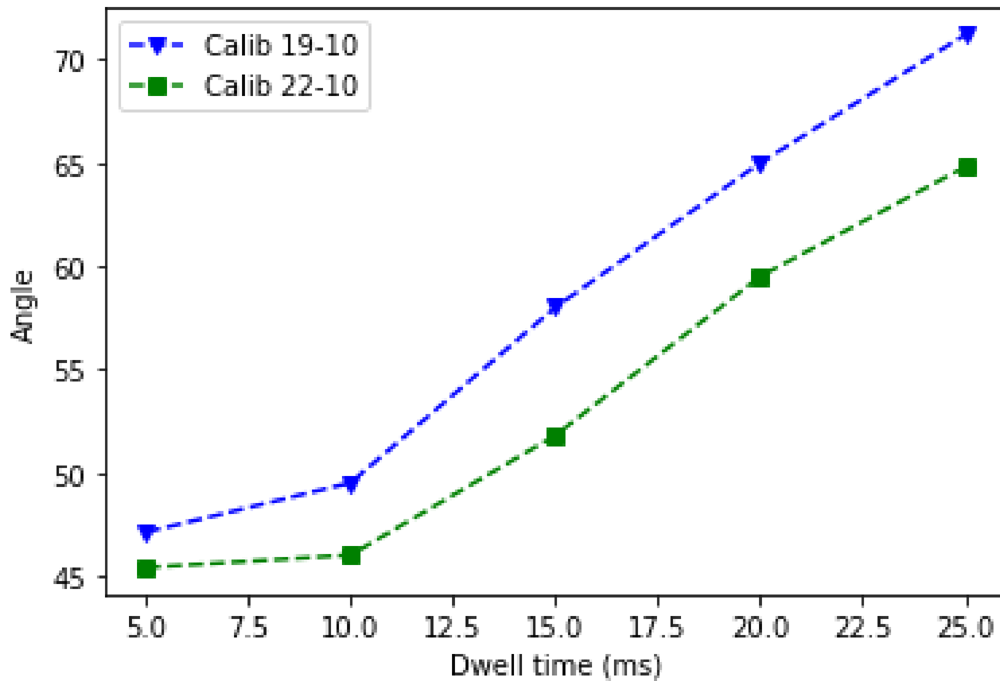

Figure 3.4: *Angle vs dwell time plot for data from two separate days. Dwell times of 5, 10, 15, 20 and 25 ms have been used. The curves have a similar shape; only a shift in values differs them.*

with connecting segments, each with a different dwell time, and use the angle tool to measure up the angle. This is illustrated in figure 3.3. Note that the beam displacement and segment size need to be the same. The effect of the beam displacement on the angle at a constant dwell time is also shown in this figure. The angle that was measured is not ζ however, but a 90° rotation. The experiment was done on two separate days, obtaining two dwell vs angle graphs, shown in figure 3.4. The shapes are the same, but the values are shifted compared to each other. This difference might be due to a combination of a day-to-day variation and a varying working pressure inside the SEM (more on this in section 3.3). The blue curve has data only from one segment per dwell time, as opposed to the green curve, which has data averaged from three segments per dwell. As the latter has more statistics, that curve is chosen as calibration curve in the CAD program.

3.3 Vertical growth rate

The average vertical growth rate (VGR) can be determined from depositing pillars. The VGR is simply the height divided by the time it takes. However, there is a slight complication. The height of the pillars depends on the SEM pressure. An initial graph of height vs pressure is shown in figure 3.5. An explanation for this effect might be the scattering of primary electrons off of the oxygen and nitrogen molecules. This scattering then effectively lowers the amount of electrons unto the substrate, and therefore the electron current. From section 2.3.1 we know that a lower current leads to less vertical growth. From the plot it is clear that there is a saturation in height. This saturation value will be used in the CAD program as the value for the VGR.
Taking only the last four points into account, the average pillar height is approximately 3.67 μm. The pillars were deposited in 6 minutes, using a dwell time of 5 ms (the amount of steps was kept constant). This yields a growth rate of $10.20 \pm 1.675 \cdot 10^{-3}$ nm/s. To account for

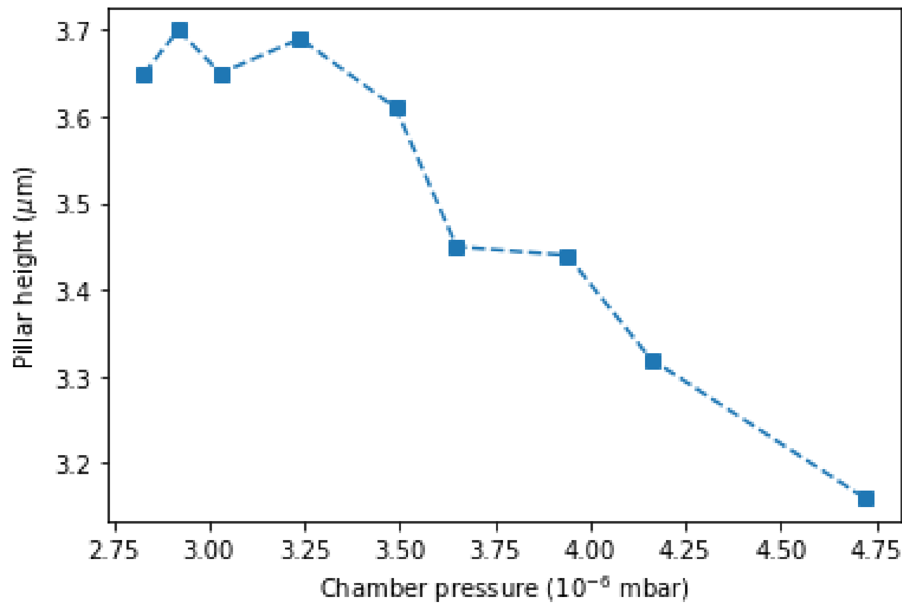

Figure 3.5: *Pillar height as a function of SEM chamber pressure. Dwell time was kept constant at 5 ms. At lower pressures, a saturation in height is visible.*

human error in measuring the precise height of the pillar, the VGR is simply put to 10 in the CAD program. There it is used to calculate the total dwell time needed to deposit a pillar with a height set by the user in the program, using the formula $\tau = \frac{L_z}{VGR}$ [13]. With this approximation at most a 10% increase in height should be observed after deposition. This can be used as a feedback loop, optimizing the streamfile with every experiment, to obtain the exact dimensions of the desired structure. Another feedback mechanism is discussed in section 3.6.
As said earlier, this plot was an initial experiment to obtain the VGR and examine the pressure dependency. Later, the experiment was done more rigorously together with a colleague. The graphs are shown in figure 3.6. The left plot shows the height of a pillar as a function of pressure, different compared to figure 3.5 only in the amount of steps, taking a pillar 3 minutes to grow. Next to it is a similar plot for the width of a spot (extremely short pillar). The growth rate as a function of number of steps at constant pressure was investigated as well and is shown in appendix A.1.

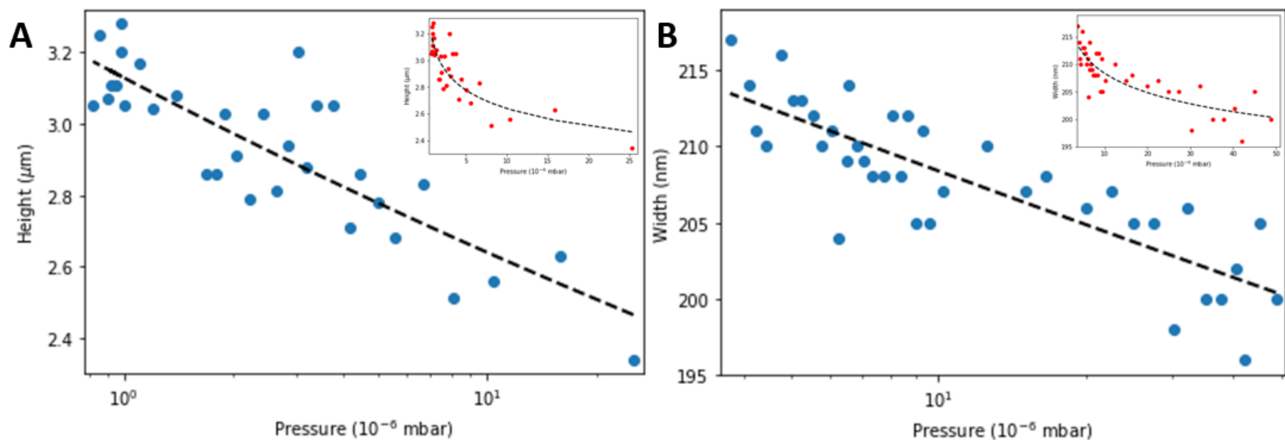

Figure 3.6: *Pressure dependency of (a) pillar height and (b) spot width, shown on a semi-log scale. The dashed line is a power law fit to the data. The inset shows the same, but on a linear scale. For (a) the error for each point is roughly 50 nm and for (b) it is 2 nm.*

3.4 Pixel point pitch and exposure pattern pixel size

In the CAD program there are two free parameters: the pixel point pitch (PoP) and the exposure pattern pixel size (iPoP). The PoP value influences the deposition via the scanning speed of the electron beam. The iPoP value gives the lowest value for the pixel point pitch, which is usually the same. It is also used in the calculation of the magnification that should be used during deposition (highlighted yellow in figure 3.2d). Their effect is captured in the following two formulas:

$$v_b = \frac{\Lambda}{\tau_d} \tag{3.1a}$$

$$Magnification = \frac{(Mag^*HFW) \cdot 10^3}{2^{bit} \cdot iPoP} \tag{3.1b}$$

In the first formula, v_b is the scanning speed, τ_d the dwell time and Λ the pixel point pitch. The second formula uses three parameters from the calibration file; the patterning bit depth, Mag*HFW and the value for the iPoP.

Before optimizing this value for a simple arch, note that the useful PoP values range from 0.2 to 2, according to Ref. 13. In figure 3.7 arches are shown, deposited using streamfiles created with the CAD program, each with a different PoP value. The first five arches are well-made, giving a range of usable values between 0.4 and 0.6 nm, well below the 2 nm, in line with suggested values by Fowlkes *et al.*[13]. When the pixel point pitch is increased more, the segments will collapse and debris will form on the substrate, as shown in figure 3.7f. Choosing a set PoP value for all arches to be deposited in the current set-up is mandatory with regard to reproducibility. The value chosen in this research is 0.5 nm.

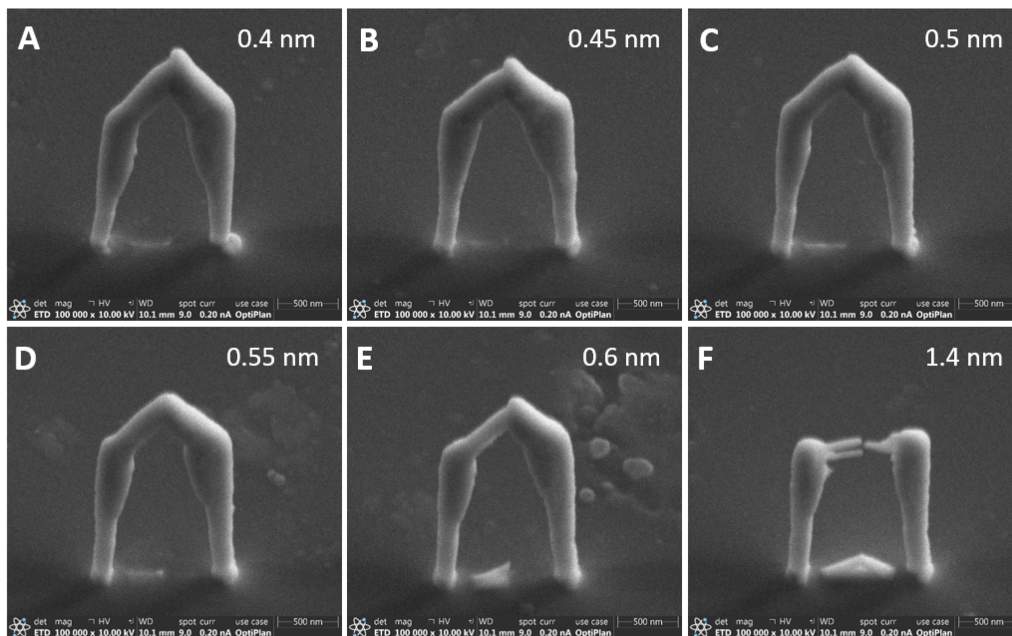

Figure 3.7: SEM pictures of arches deposited using streamfiles created with the CAD program. Different values for the pixel point pitch are used, while keeping everything else constant. Between 0.4 and 0.6 nm, the segments attach to each other. At higher values, however, the scanning speed becomes too fast and the segments collapse.

3.5 Designs

Now having obtained all the important parameters from section 3.1, the CAD program can be used to produce streamfiles of 3D structures. In this section, two designs will be presented. The first one is a simple arch, shown in figure 3.8. The second structure is a double arch. It consists of two segments on each side, with a gap between the two arches.

Figure 3.8a, showing the design in the CAD program, already gives away one of the flaws of the program. Namely, the visual scale which is used while creating a design. For higher currents, such as 5 nA, structures need to be bigger, up to even a few micron. This is out of reach for the visual scale, making it much more difficult to create a complicated design. The actual values used in the CAD program are much larger; pillar to pillar length and length of the feet are set to 4 μm, while the pillar height is set to 1 μm. The experiment, figure 3.8b, then shows surprisingly different dimensions. In the horizontal (x) direction, the size is halved, while in the z direction it is doubled, obtaining a two by two arch with feet of that same size. This effect is consistently seen while depositing arches. However, the cause of this effect is unknown and a matter of importance in further research on this topic.
Another effect is seen when depositing an arch on the gold contacts that are used for measurements, in figure 3.9. The feet of the arch are not straight lines anymore, but consist of multiple inclined pillars that form an distorted line. This looks similar to figure 2.7c, which indicates that the scanning speed is too low to form a line. In fact, it is experimentally verified that the vertical growth rate on Au is 1.5 times larger than on Si[64]. It can be explained by a difference in BSE and SE yields. To account for the difference in growth rate, one should indeed have a higher scanning speed.

A double arch was made using a similar procedure to that of a normal arch. Figure 3.10a-c shows the structure for three different PoP values. Notice that the range of appropriate values is considerably smaller for a double arch. This is due to the fact that the four segments are much closer to each other than in the case of a normal arch, and therefore influence each other's growth. The optimum value is 0.3 nm.

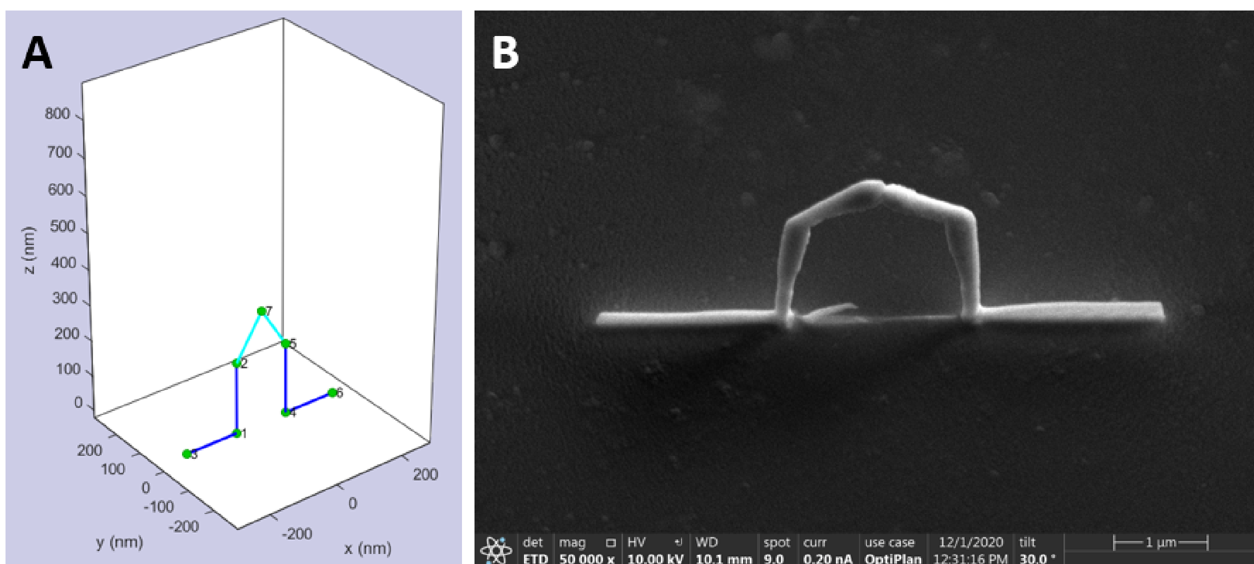

Figure 3.8: *(a) Visualization of an arch in the CAD program and (b) a SEM picture of an arch, using a streamfile made with the CAD program.*

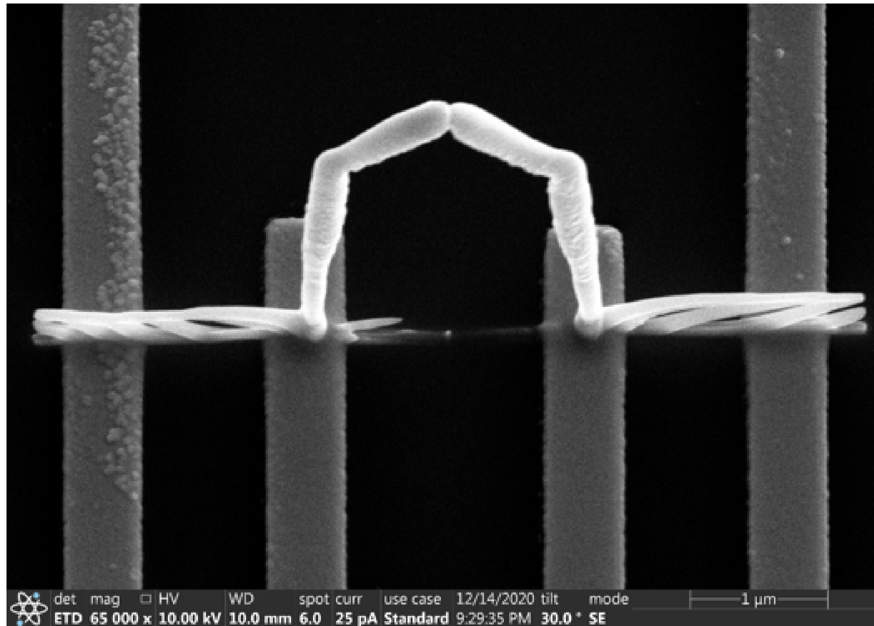

Figure 3.9: *SEM image of an arch. The fence pattern of the feet is caused by a low scanning speed w.r.t. the vertical growth rate. The gold substrate has a higher growth rate than a Si substrate, for which the settings are optimized.*

Figure 3.10d-f shows SEM pictures of the double arch taken at three different angles, displaying good beam control, especially considering how high of a current is used in the experiments.

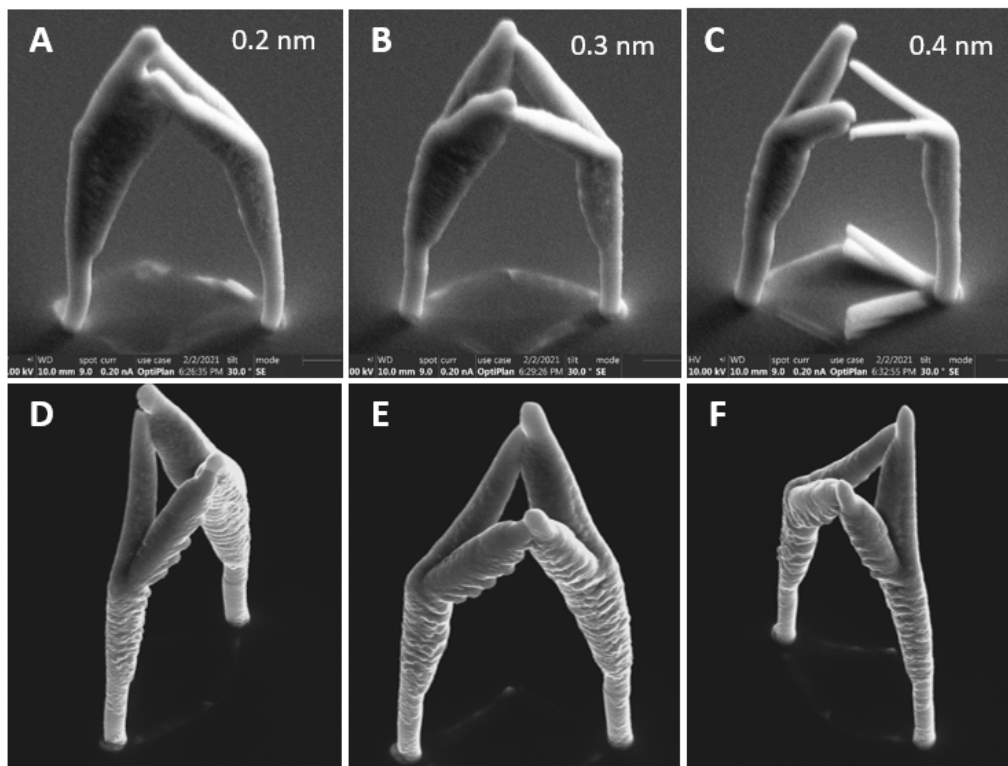

Figure 3.10: *SEM pictures of a double arch, fabricated using a streamfile made with the CAD program. The top three pictures have a different value for the pixel point pitch, showing only a narrow range of usable values for this parameter. The bottom three pictures show the double arch with a PoP value of 0.3 nm from different angles.*

3.6 Hybrid Monte-Carlo simulation

Exact solutions of complex problems in physics is in most cases unattainable. Therefore, simulations are a very useful and versatile tool in solving those problems, one of which is focused electron beam induced deposition (FEBID). One type of simulation is a Monte-Carlo simulation, which uses probability distributions to solve the problem. An advantage of this type is the straightforward implementation of strong correlation effects, such as electron-solid interactions.

The hybrid Monte-Carlo simulation from Fowlkes *et al.*[65] consists of two parts. Firstly, a Monte-Carlo simulation is run to obtain the electron trajectories through the solid-of-interest. Elastic (Rutherford) scattering and inelastic scattering are modeled in this simulation, using the screened Rutherford cross-section and a continuous energy loss approximation[66]. This gives us the position and energy of the primary electrons.
An input is given by the beam scanning coordinates and corresponding dwell times, i.e. the streamfile. This can be obtained with the CAD program. With this input, the simulation space can be divided into voxels, indicating whether it plays the part of a material surface 'S', bulk 'B' or vacuum 'V'. This initiates the second part; the FEBID simulation. When an electron passes through a 'B' voxel, inelastic scattering happens, leading to a yield of

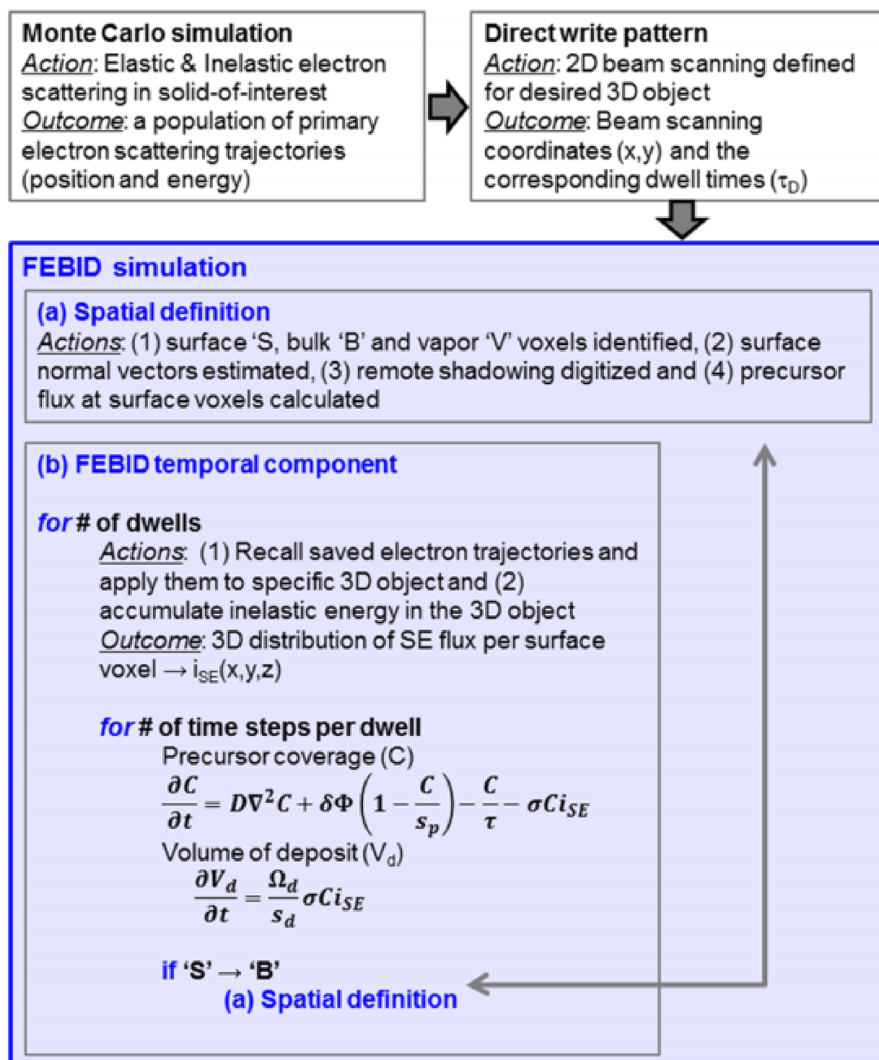

Figure 3.11: *Flow chart of the hybrid Monte-Carlo simulation. Taken from Ref. 65.*

secondary electrons. Trajectories of SE are generated and the number of SE's traversing an 'S' voxel is calculated to get the surface emission profile $i_{SE}(x, y, z)$. When an electron trajectory passes through a 'V' voxel, the trajectory is not altered until it reenters the solid. The above FEBID subroutine is performed at the start of every dwell time.
The second subroutine, however, is performed multiple times per dwell time. This subroutine entails solving a continuum rate equation describing precursor adsorption, desorption, surface diffusion, dissociation and deposition. It uses the SE surface emission profile calculated in the first subroutine. All steps are also shown in figure 3.11 above.

The above simulation can give feedback to designs made with the CAD program. This allows for a massive improvement in streamfiles, without the use of additional fine-tuning experiments (section 3.4). Note that in this project the structures were relatively large, mainly due to the relatively large beam current of 5 nA. To then improve on the simulation, the effect of beam defocus has to be implemented, which is absent in the current version.

CHAPTER 4

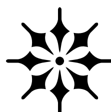

TRANSPORT MEASUREMENTS OF EBID NANOSTRUCTURES

This chapter shows and discusses results of transport measurements on 3D nanostructures made with EBID. Also, the atomic contents of an arch has been obtained using EDX measurements (appendix A.2).

4.1 Resistance curves & critical temperature

Transport measurements were conducted on three arches with a size of roughly 2x2 μm^2 (see section 3.5). Resistance as function of temperature is plotted first to see whether the arches exhibit superconducting behaviour. One of the arches, fabricated using a combination of the CAD program and the line function from the SEM itself, was in connection with one of the other arches, that were made fully with the CAD program. This "hybrid" arch is excluded from any data analysis, however, a superconducting transition can already be seen in figure 4.1, where resistance curves are plotted for different values of the magnetic field, applied in the positive x-direction w.r.t. the arches in the SEM pictures. In fact, best seen at low magnetic fields, there are multiple transitions, indicating an inhomogeneous structure. This is also implied by the rather wide superconducting transition.

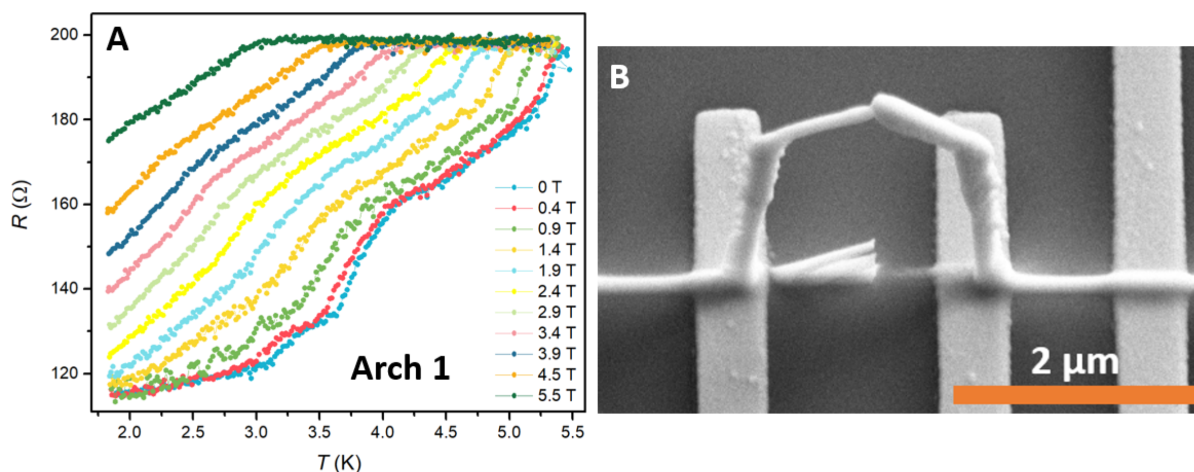

Figure 4.1: *(a) Resistance of a tungsten arch deposited with EBID as a function of temperature, plotted for different values of the applied magnetic field. Measured with an AC current of 1 μA. (b) A SEM picture of the same arch, using a streamfile made with the CAD program.*

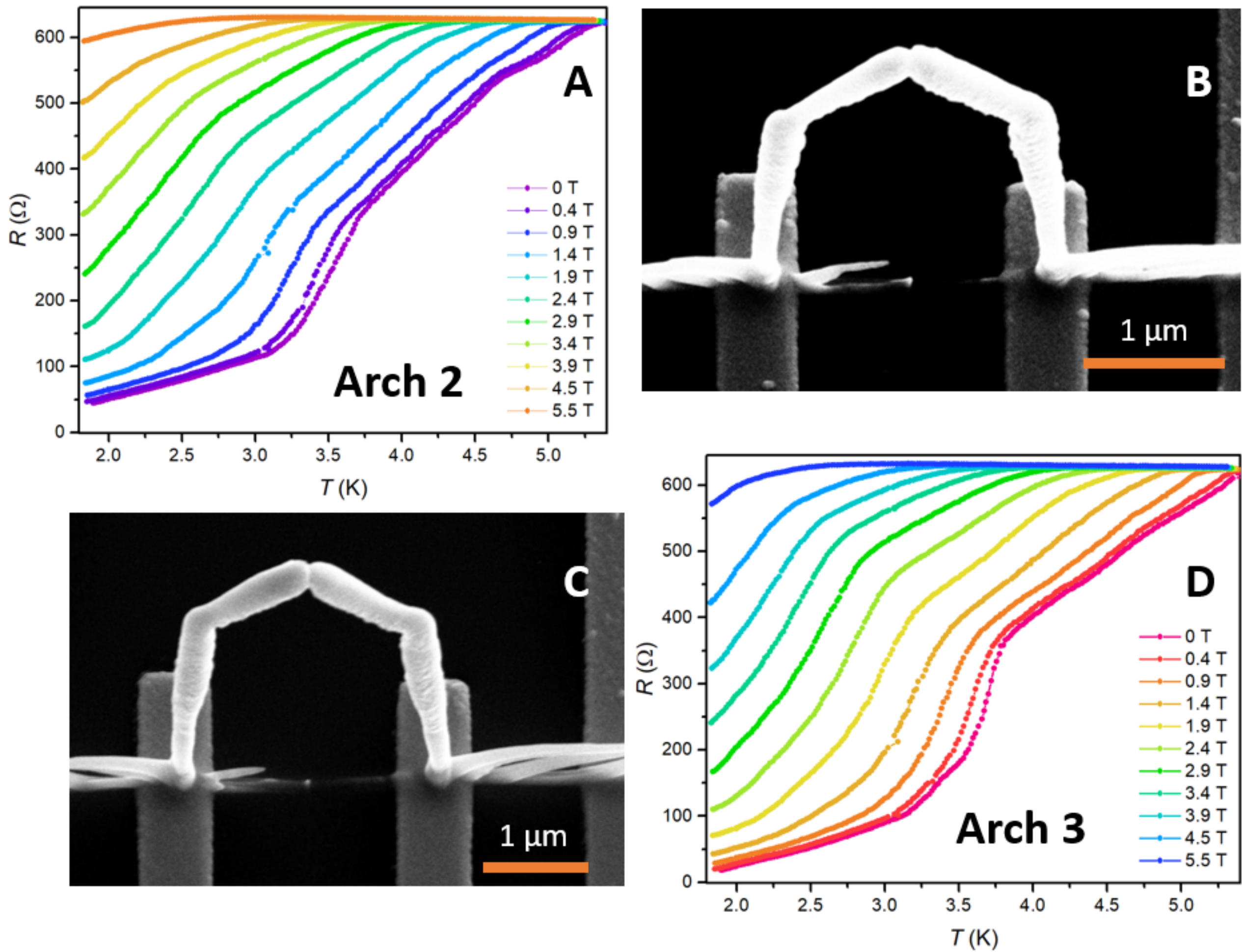

Figure 4.2: *Resistance of a tungsten arch deposited with EBID as a function of temperature, plotted for different values of the applied magnetic field. Both samples exhibit superconducting behaviour, decreasing their resistance to (a) 45 Ω and (d) 19 Ω. Measured with a DC and AC current of 1 μA respectively. Also shown are the SEM pictures of the corresponding arches, (b) and (c) respectively.*

Figure 4.2 shows the other arches with their corresponding resistance curves. At the lowest temperature reached with the cryostat (1.9 K), they show a resistance of 45 Ω (4.2a) and 19 Ω (4.2d). It is clear that although the arches show superconducting behaviour, the resistance will not drop to zero as expected. An explanation for this residual resistance is given in Ref. 67. In short, when depositing in alternating mode, resistive debris is formed away from the irradiation spot. With an arch as example, this means that when creating the pillars or segments, a layer of resistive material will form on the pillar/segment that is not directly irradiated by the electron beam. Eventually, the structure will consist of alternating layers of conductive material and resistive material.

From these resistance curves one can obtain the critical temperature of the structure for every value of the magnetic field. The critical temperature, T_c, is usually defined by the point where resistance is reduced by 90% or at the halfway point. The latter is only viable when a sharp transition occurs. For the two arches, three different values of the resistance are taken to provide three curves, shown in figure 4.3 as dots. The Ginzburg-Landau relation $T_c(B) = T_c(0)[1 - (\frac{B(T)}{B(0)})^2]$ then provides the fit curves, indicated by the solid lines. In this formula, $T_c(0)$ is the critical temperature at zero magnetic field, and $B(0)$ is the value of the critical magnetic field at zero K, which is obtained by fitting. The magnetic field corresponding to a certain critical temperature as seen in figure 4.3 is actually the second critical field,

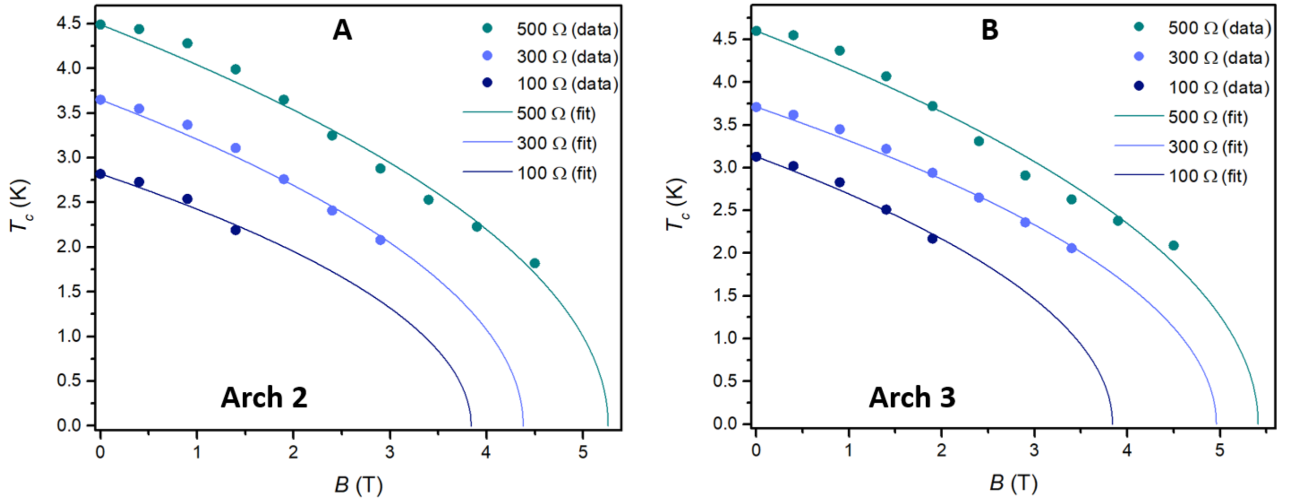

Figure 4.3: *Critical temperature as a function of applied magnetic field. Data is taken from three different values of the resistance and plotted for both arches separately. Fits were made using the Ginzburg-Landau relation as described in the text.*

$B_{c,2}$. As the resistance curves are very broad, easily spanning a range of critical temperatures from 2 to 5 K, one needs to be careful as to which definition of T_c to use. Therefore, calculations of coherence length and penetration depth, and subsequently also the Ginzburg-Landau parameter, $\kappa \equiv \lambda/\xi$, are done for all three cases to see how much they differ.

4.1.1 Calculation of Ginzburg-Landau parameter

Calculating the coherence length, $\xi(T)$, is quite simple using the formula

$$B_{c,2}(T) = \Phi_0/2\pi\xi^2(T), \tag{4.1}$$

together with the Ginzburg-Landau (GL) relation for B(T). As the GL parameter varies slowly with temperature, it is sufficient to take it as constant in the range of the measured temperatures, needing only the zero K values of the coherence length, $\xi(0)$, and penetration depth, $\lambda(0)$. The values are accumulated in table 4.1.

Table 4.1: *Values of important quantities in transport measurements for two superconducting arches.*

Arch	Resistance	$T_c(0)$[1]	$B(0)$[2]	$\xi(0)$[3]	$\lambda(0)$[3]	κ[3]
2	500 Ω	4.49 K	5.26 ± 0.09 T	7.91 nm	991 nm	125
2	300 Ω	3.65 K	4.38 ± 0.11 T	8.67 nm	1099 nm	127
2	100 Ω	2.82 K	3.84 ± 0.32 T	9.26 nm	1251 nm	135
3	500 Ω	4.60 K	5.41 ± 0.12 T	7.80 nm	1043 nm	134
3	300 Ω	3.71 K	4.96 ± 0.08 T	8.15 nm	1162 nm	143
3	100 Ω	3.13 K	3.84 ± 0.17 T	9.26 nm	1265 nm	137

[1] Obtained from data.
[2] Obtained from fit.
[3] Calculated.

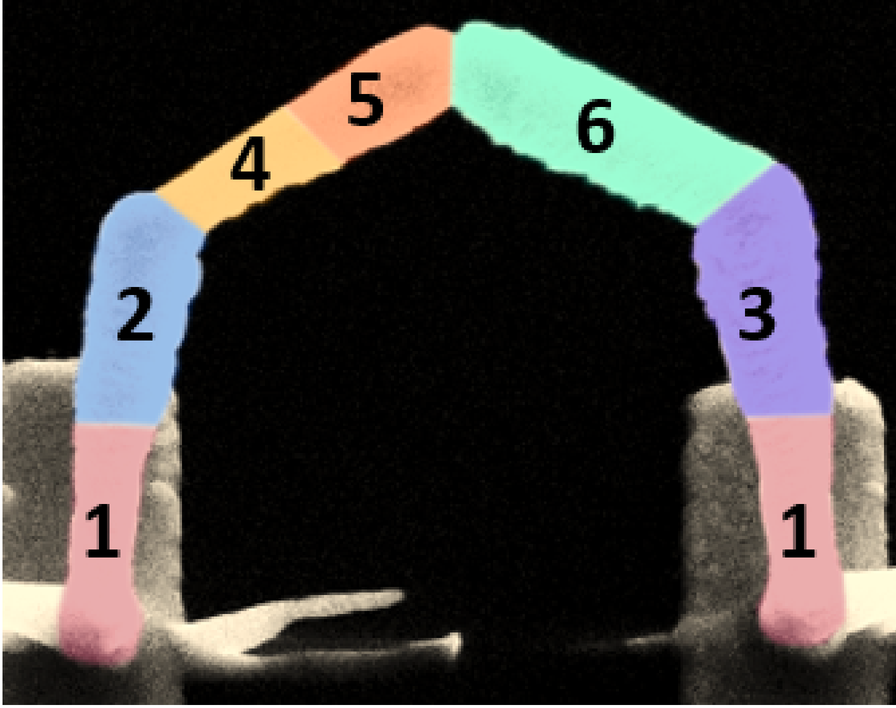

Figure 4.4: *False-coloured SEM image of arch 2. The numbers indicate parts with different lengths and/or radii. This is used to calculate the penetration depth more precisely.*

The penetration depth is a bit more complicated to calculate, owing to the exact shape of the arch. The formula used here is the following:[68]

$$\lambda(0) = 1.05 \cdot 10^2 \sqrt{\rho / T_c} \tag{4.2}$$

Here, λ is in nm, the resistivity ρ in $\mu\Omega$ cm and T_c is in K. The resistivity is linked to the dimensions of the arch. For this purpose, the arch is divided up into multiple wires with different radii and lengths. A false-coloured image of arch 2 shows the used division (figure 4.4). Using the resistance value before the transition, we get a resistivity of approximately 400 $\mu\Omega$ cm. The same is done for arch 3, obtaining a resistivity of 454 $\mu\Omega$ cm.

Given that values for B(0) and $\xi(0)$ for both arches are the same, indicates that the definition of T_c at 100 Ω is the more correct value. Also the values for the penetration depth, $\lambda(0)$ and GL parameter, κ are very close to each other. On the other hand, the data at 100 Ω constitutes of only a handful of points, about half of the data at higher resistances. To make a stronger case, clearly, one must go to lower temperatures (around 300 mK) and take smaller steps between different magnetic fields.

4.2 Current characteristics

Unmissable in transport measurements are I-V curves and, in the case of superconductivity, also obtaining the critical current as function of temperature. These current characteristics could only be obtained for arch 2, and are shown in figures 4.5 and 4.6.
Firstly, the I-V curve in figure 4.5 gives us a measure of the resistance at the documented temperatures. This leads to a slightly lower resistance (42 Ω) than from figure 4.2a (45 Ω).
Secondly, figure 4.6a shows the differential resistance as function of current. In this plot, the critical current is defined as the highest peak in the curve. Only six curves are shown

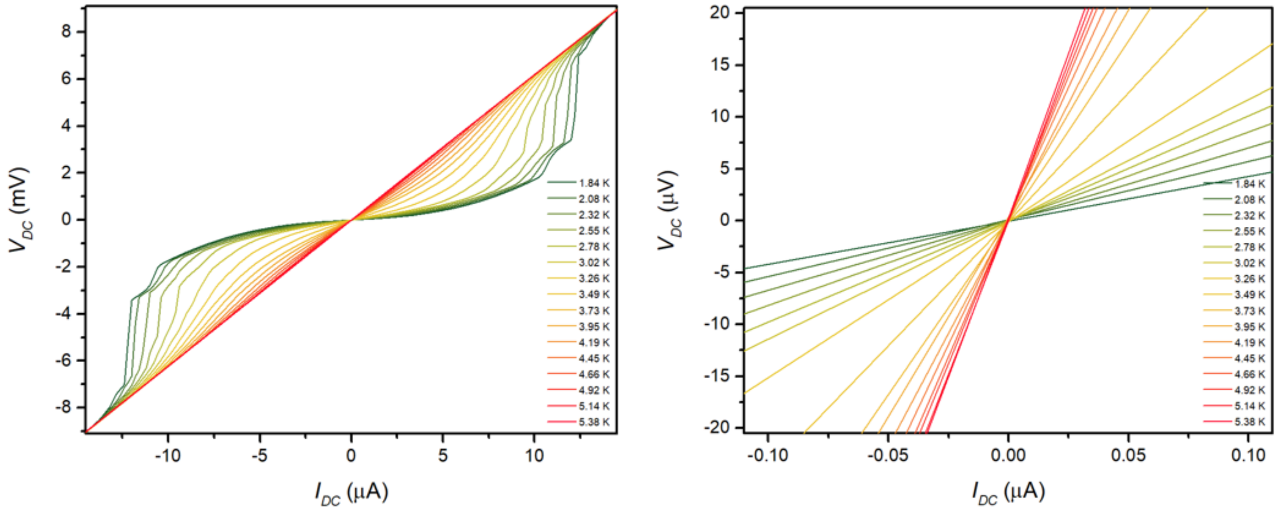

Figure 4.5: *Voltage as function of current for multiple temperatures, starting from 1.84 K up to 5.38 K. Figure (a) shows the full curve, whereas (b) shows the zoomed in curve. At low current Ohmic behaviour is seen, and thus from the slope the resistance can be obtained. At the lowest temperature this becomes 42.3 Ω.*

(corresponding to six different temperatures), because at higher temperatures, the curves are all more or less flat.
Finally, a plot of the critical current as function of temperature is obtained, shown in figure 4.6b. The points are fitted to the following empirical law:[69]

$$I_c(T) = I_c(0)\left[1 - \left(\frac{T}{T_c}\right)^2\right] \tag{4.3}$$

The critical temperature, T_c, was not taken from data, but was also taken as a fit parameter, together with $I_c(0)$. Values obtained are $T_c \approx 4.77 \pm 6.52 \cdot 10^{-2}$ K and $I_c(0) \approx 14.51 \pm 0.15$ μA. The critical temperature is higher than expected from data (see figure 4.3). The fit itself is fairly decent, but does not match perfectly with the data points.

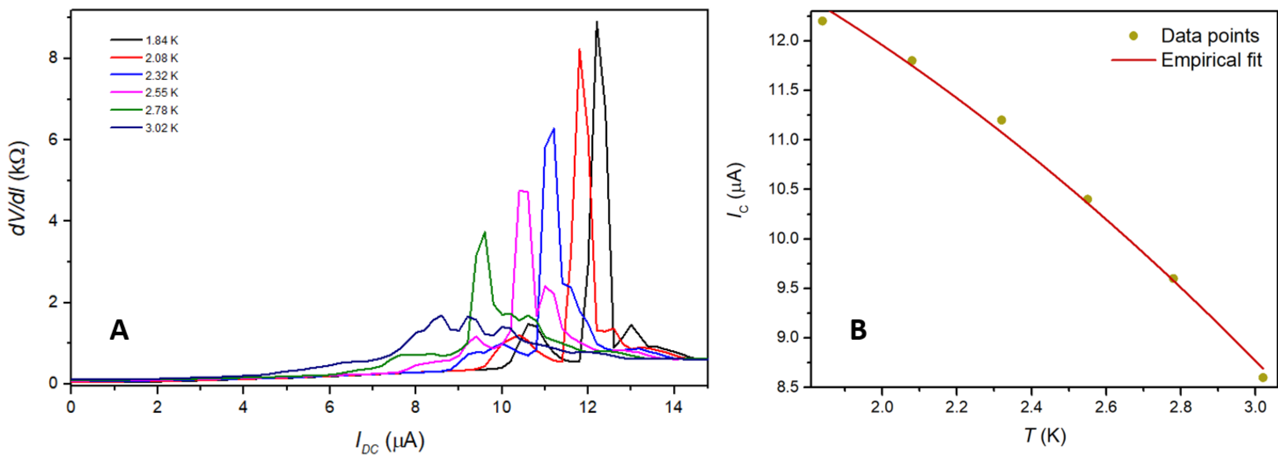

Figure 4.6: *(a) Differential resistance as function of current, where the peaks in the curves denote the critical current. (b) The critical current as function of temperature, fitted to the empirical law from equation 4.3. The empirical fit gives $T_c \approx 4.77 \pm 6.52 \cdot 10^{-2}$ K and $I_c(0) \approx 14.51 \pm 0.15$ μA.*

.

The definition of critical temperature and current hugely influences the perception of the data. Couple this to the relatively sparse data points, with temperatures down only to 1.9 K, and this gives a possible explanation of why the values for the critical temperature are different. It also explains the quality of the fitting curve.

Looking back at the last two chapters, we managed to fabricate a superconducting arch using a CAD program, new to our research group. In this way, superconducting arches were made in a third of the time compared to previous (successful) attempts. A more complex arch was also made, showing the beam control with the new program. This paves the way to even more complex structures, aided by simulations.

CHAPTER 5

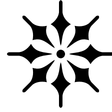

CONCLUSION & OUTLOOK

The conclusions are presented in bullet point format and per section. The outlook is treated in a similar way.

5.1 Conclusion

- A thorough summary of EBID experiments reveals that it is a very complex interplay between electrons, substrate and deposit. Although a lot is known and understood, there is still plenty to learn (chapter 2).

- Making streamfiles with the computer aided design (CAD) program from Ref. 13. requires two calibration files to work; one with an angle versus dwell time plot and a list of specific parameters. The vertical growth rate (VGR) and the correct pixel point pitch (PoP) value have to be submitted as well (section 3.1).

- The list of specific parameters are shown in table 3.1. The angle versus dwell time plot is shown in figure 3.4. The difference between the two curves is most likely caused by a combination of day-to-day variation and a varying working pressure (section 3.2).

- The graph with pillar height as a function of chamber pressure is shown in figure 3.5 The saturation in this plot leads to an approximate VGR of 10 nm/s. The saturation could occur due to a lack of statistics. A later, more rigorous experiment about the pressure dependency of the pillar height shows no saturation. It reveals, however, a new dependency on the number of steps executed to form the pillar (section 3.3).

- For the arch, choosing a PoP value in the range of 0.4-0.6 nm leads to a nicely-shaped arch. Below or above these values, the arch collapses. For optimization, a value of 0.5 nm is chosen (section 3.4).

- With all the previous experiments done, all values can be submitted into the CAD program. The dimensions of the arch in the program and the final product made by the SEM (figure 3.8) are not the same. It is currently unknown what causes the differences. Using the same settings for the feet of the arch on gold (i.s.o Si) leads to a fence-like structure (figure 3.9). This is caused by a low scanning speed of the beam relative to a Si substrate. A double arch was also designed and made (figure 3.10), optimized using a PoP value of 0.3 nm (section 3.5).

- The hybrid Monte-Carlo simulation from Ref. 65 is very beneficial to have as a feedback loop to optimize streamfiles made with the CAD program (section 3.6).

- Transport measurements were done only on the normal arches. Their resistance curves are shown in figure 4.2. At the lowest temperature, the resistances are 45 Ω and 19 Ω, which is not zero as should be expected from superconductivity. This is due to a relatively high cryostat temperature; the arches are not yet fully in superconducting mode. Secondly, there exists a residual resistance in arches made with EBID[67]. From the resistance curves, the critical temperature as a function of magnetic field is extracted. Together with the formulae 4.1 and 4.2, a table of important quantities was made (table 4.1). These quantities varied with every different definition of the critical temperature. It was found that for the two arches (Arch 2 and Arch 3 in the text) that the coherence length and penetration depth are very close to each other in value at a defining critical temperature based on a resistance of a 100 Ω. Therefore, this seems like the correct definition. More experiments have to be done in order to make a stronger case (section 4.1).

- Figure 4.6a shows the differential resistance as function of the current, defining a critical current at the highest peak in the curves. These are then plotted in figure 4.6b, together with a fit to the empirical law from equation 4.3. This yields a fairly decent fit with fitting parameters $T_c \approx 4.77 \pm 6.52 \cdot 10^{-2}$ K and $I_c(0) \approx 14.51 \pm 0.15$ μA. The slight mismatch can be explained by a lack of data points and the definition of the critical temperature and current (section 4.2).

- The main improvement in superconducting arches compared to previous attempts is the huge decrease in fabrication time (section 4.2).

5.2 Outlook

- From experiments it is clear that the VGR is not constant; it depends on the SEM pressure and the number of dwell times. Therefore, characterization of these effects and implementation of a separate VGR value in the CAD program per segment/pillar will improve on the fabricated structures.

- An extended visual scale in the CAD program will benefit fabrication of complex structures immensely. Changing the axes on the visual scale as you see fit should be implemented into the program.

- The mismatch between the design and the experiment should be investigated. A great tool for this would be a simulation, as talked about in section 3.6.

- To improve on the simulation, the effect of defocus should be taken into account, as the structures made in this project are relatively large.

- Measurements can be improved by doing magnetic field sweeps at a much lower temperature, around 300 mK. Smaller increments between the magnetic field values will add to the statistics, improving the data quality even further.

Appendix A

A.1 Pillar height dependency

As seen from previous experiments, the number of dwell times (steps) needed to fabricate a pillar, influences the height of the pillar in a non-linear way. Therefore, an experiment was set up to investigate this effect. The pressure was kept constant in a range of 1.69-1.82$\cdot 10^{-6}$ mbar. The results are shown in figure A.1 below, together with a SEM image of one of the pillars.

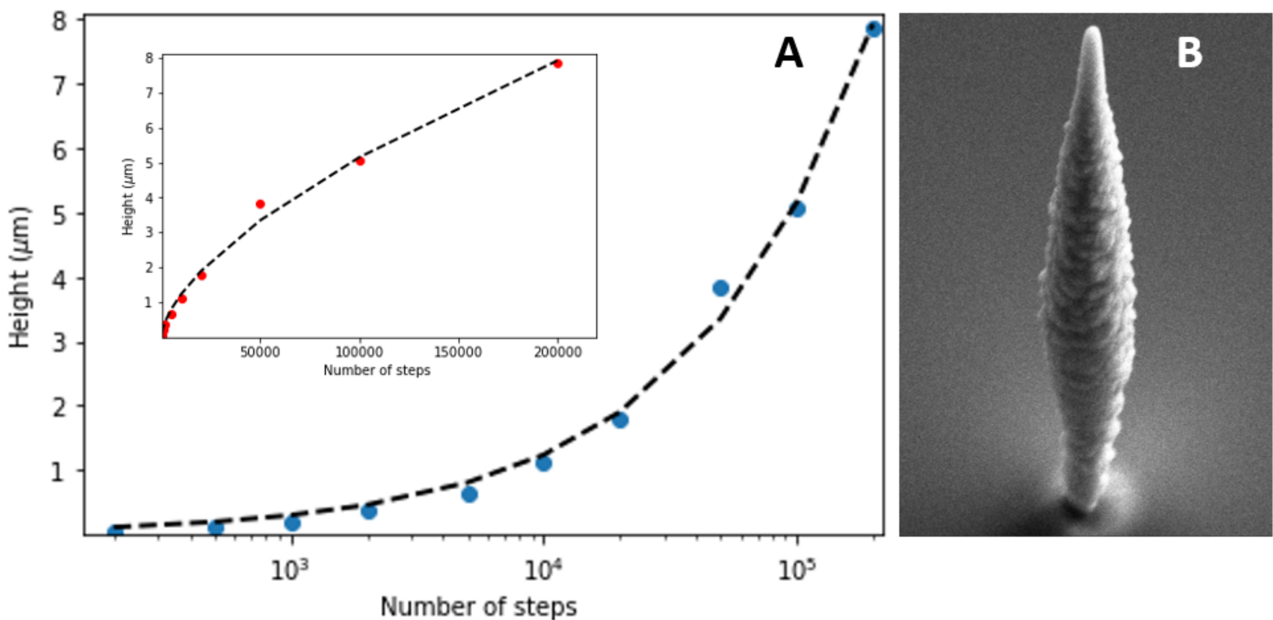

Figure A.1: *(a) The dependency of the pillar height on the number of steps on a semi-log plot. The inset shows the same data, but on a linear scale. The dashed line is a power law fit. (b) SEM image of one of the pillars, made with 50.000 steps with a dwell time of 5 ms.*

.

A.2 EDX measurement

With EDX the atomic contents of a material can be obtained. Results for an arch are presented in the table below.

Table A.1: *Atomic percentages of tungsten for different parts of an arch.*

Part of arch	Percentage W
Top of segment	28-30%
Middle of segment	24-25%
Top of left pillar	30%
Bottom of left pillar	27%
Middle of right pillar	31%

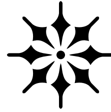

ACKNOWLEDGEMENTS

I would like to thank Jan Aarts for letting me do a project in his group. I also want to thank Kaveh for the daily supervision. I really appreciate the help that I got from Remko, with the measurement and wire bonding the samples. And also the help from Thomas whenever the SEM had problems. So thank you. Last but not least, I am grateful for the pleasant atmosphere which was present in room HL628. Special thanks to my room mates Timothy, Dyon and Naor.

This research was made possible by financial support from the Dutch Association for Scientific Research (NWO) and the Foundation for Fundamental Research of Matter (FOM).

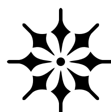

Bibliography

[1] Hao, L. *et al.* Measurement and noise performance of nano-superconducting-quantum- interference devices fabricated by focused ion beam. *Applied Physics Letters* **92** (2008).

[2] Di Iorio, M. S. *et al.* Practical high Tc Josephson junctions and dc SQUIDs operating above 85 K. *Applied Physics Letters* **58**, 2552–2554 (1991).

[3] Sattelkow J *et al.* 3D nano-thermistors for thermal probing. *ACS Applied Materials and Interfaces (unpublished)* .

[4] Winkler, R. *et al.* Direct-Write 3D Nanoprinting of Plasmonic Structures. *ACS Applied Materials and Interfaces* **9**, 8233–8240 (2017).

[5] Keller, L. *et al.* Direct-write of free-form building blocks for artificial magnetic 3D lattices. *Scientific Reports* **8** (2018).

[6] Sanz-Hernández, D. *et al.* Fabrication of scaffold-based 3D magnetic nanowires for domain wall applications. *Nanomaterials* **8** (2018).

[7] Sanz-Hernández, D. *et al.* Fabrication, Detection, and Operation of a Three-Dimensional Nanomagnetic Conduit. *ACS Nano* **11**, 11066–11073 (2017). 1706.03710.

[8] Al Mamoori, M. K. *et al.* Magnetic characterization of direct-write free-form building blocks for artificial magnetic 3D lattices. *Materials* **11** (2018).

[9] Vavassori, P. *et al.* Remote Magnetomechanical Nanoactuation. *Small* **12**, 1013–1023 (2016).

[10] Arnold, G. *et al.* Tunable 3D Nanoresonators for Gas-Sensing Applications. *Advanced Functional Materials* **28** (2018).

[11] Esposito, M. *et al.* Nanoscale 3D chiral plasmonic helices with circular dichroism at visible frequencies. *ACS Photonics* **2**, 105–114 (2015).

[12] Passaseo, A. *et al.* Materials and 3D Designs of Helix Nanostructures for Chirality at Optical Frequencies (2017).

[13] Fowlkes, J. D. *et al.* High-Fidelity 3D-Nanoprinting via Focused Electron Beams: Computer-Aided Design (3BID). *ACS Applied Nano Materials* **1**, 1028–1041 (2018).

[14] Winkler, R. *et al.* 3D nanoprinting via focused electron beams. *Journal of Applied Physics* **125** (2019).

[15] Li, W. *et al.* Superconductivity of ultra-fine tungsten nanowires grown by focused-ion-beam direct-writing. *Microelectronic Engineering* **88**, 2636–2638 (2011).

[16] Van Dorp, W. F. *et al.* A critical literature review of focused electron beam induced deposition. *Journal of Applied Physics* **104** (2008).

[17] Fowlkes, J. D. *et al.* Growth and simulation of high-aspect ratio nanopillars by primary and secondary electron-induced deposition. *Journal of Vacuum Science & Technology B: Microelectronics and Nanometer Structures* **23**, 2825 (2005).

[18] Mølhave, K. *et al.* Solid Gold Nanostructures Fabricated by Electron Beam Deposition. *Nano Letters* **3**, 1499–1503 (2003).

[19] Kohlmann-von Platen, K. T. Resolution limits in electron-beam induced tungsten deposition. *Journal of Vacuum Science & Technology B: Microelectronics and Nanometer Structures* **11**, 2219 (1993).

[20] Perentes, A. *et al.* Focused electron beam induced deposition of a periodic transparent nano-optic pattern. *Microelectronic Engineering* **73-74**, 412–416 (2004).

[21] Beaulieu, D. *et al.* Influence of process variables on electron beam chemical vapor deposition of platinum. *Journal of Vacuum Science & Technology B: Microelectronics and Nanometer Structures* **23**, 2151 (2005).

[22] Utke, I. *et al.* High-resolution magnetic Co supertips grown by a focused electron beam. *Applied Physics Letters* **80**, 4792–4794 (2002).

[23] Schiffmann, K. I. Investigation of fabrication parameters for the electron-beam-induced deposition of contamination tips used in atomic force microscopy. *Nanotechnology* **4**, 163–169 (1993).

[24] Hoyle, P. C. Electron beam induced deposition from $W(CO)_6$ at 2 to 20 keV and its applications. *Journal of Vacuum Science & Technology B: Microelectronics and Nanometer Structures* **14**, 662 (1996).

[25] Shimojo, M. *et al.* Nanodot and nanorod formation in electron-beam-induced deposition using iron carbonyl. *Japanese Journal of Applied Physics, Part 1: Regular Papers and Short Notes and Review Papers* **44**, 5651–5653 (2005).

[26] Silvis-Cividjian, N. *et al.* The role of secondary electrons in electron-beam-induced-deposition spatial resolution. *Microelectronic Engineering* **61-62**, 693–699 (2002).

[27] Hübner, U. *et al.* On-line nanolithography using electron beam-induced deposition technique. *Microelectronic Engineering* **57-58**, 953–958 (2001).

[28] Rowntree, P. *et al.* Anion Yields Produced by Low-Energy Electron Impact on Condensed Hydrocarbon Films. *J. Phys. Chem* **95**, 4902–4909 (1991).

[29] Hirsch, E. H. Image formation by electron bombardment of metal targets Related content Image formation by electron bombardment of metal targets. *British Journal of Applied Physics* **11**, 547–550 (1960).

[30] Mezhenny, S. *et al.* Electron stimulated decomposition of adsorbed hexafluoroacetylacetonate Cu(I) vinyltrimethylsilane, Cu(I)(hfac)(vtms). *Journal of Applied Physics* **85**, 3368–3373 (1999).

[31] George, P. M. *et al.* Deposition of metal fllms by the controlled decomposition of organometallic compounds on surfaces. *Thin Solid Films* **67**, L25–L28 (1980).

[32] Rowntree, P. Chemical Processes of Electron Beam Induced Deposition. *Presented at the First International EBID Workshop, Delft (unpublished)* (2006).

[33] Henderson, M. *et al.* Low-energy electron induced decomposition of $Fe(CO)_5$ adsorbed on Ag(111). *Surface Science* **259**, 173–182 (1991).

[34] Tian, C. *et al.* Cross sections of the electron impact dissociative ionization of CO, CH_4 and C_2H_2. *Journal of Physics B: Atomic, Molecular and Optical Physics J. Phys. B: At. Mol. Opt. Phys* **31**, 895–909 (1998).

[35] Hoyle, P. C. *et al.* Ultralow-energy focused electron beam induced deposition. *Applied Physics Letters* **64**, 1448–1450 (1994).

[36] Takai, M. *et al.* Processing of vacuum microelectronic devices by focused ion and electron beams. *Applied Physics A: Materials Science and Processing* **76**, 1007–1012 (2003).

[37] Bauerdick, S. *et al.* In-situ monitoring of electron beam induced deposition by atomic force microscopy in a scanning electron microscope. *Microelectronic Engineering* **67-68**, 963–969 (2003).

[38] Lipp, S. *et al.* A COMPARISON OF FOCUSED ION BEAM AND ELECTRON BEAM INDUCED DEPOSITION PROCESSES. *Microelectron. Reliab* **36**, 1779–1782 (1996).

[39] Randolph, S. J. *et al.* Effects of heat generation during electron-beam-induced deposition of nanostructures. *Journal of Applied Physics* **97** (2005).

[40] Naruhisa Miura *et al.* Application of Carbonaceous Material for Fabrication of Nano-Wires with a Scanning Electron Microscopy. *Japanese Journal of Applied Physics* **35**, L1089–L1091 (1996).

[41] Kohlmann-von Platen, K. T. Electron-beam induced tungsten deposition: Growth rate enhancement and applications in microelectronics. *Journal of Vacuum Science & Technology B: Microelectronics and Nanometer Structures* **10**, 2690 (1992).

[42] Gopal, V. *et al.* Metal delocalization and surface decoration in direct-write nanolithography by electron beam induced deposition. *Applied Physics Letters* **85**, 49–51 (2004).

[43] Reimer, L. *Scanning Electron Microscopy* (Springer-Verlag, Berlin, 1998).

[44] Fourie, J. T. The Controlling Parameter in Contamination of Specimens in Electron Microscopes. *Optik* **44**, 111–114 (1975).

[45] Reimer, L. *et al.* Contribution to the Contamination Problem in Transmission Electron Microscopy. *Ultramicroscopy* **3**, 169–174 (1978).

[46] Amman, M. *et al.* Atomic force microscopy study of electron beam written contamination structures. *Journal of Vacuum Science & Technology B: Microelectronics and Nanometer Structures* **14**, 54 (1996).

[47] Utke, I. *et al.* Resolution and Growth Regimes in Focused Ion and Electron Beam Induced Processing. *Journal of Vacuum Science & Technology B (submitted)* .

[48] Smith, D. A. *et al.* A nanoscale three-dimensional Monte Carlo simulation of electron-beam-induced deposition with gas dynamics. *Nanotechnology* **18** (2007).

[49] Lipp, S. *et al.* Tetramethoxysilane as a precursor for focused ion beam and electron beam assisted insulator (SiOx) deposition. *Journal of Vacuum Science & Technology B: Microelectronics and Nanometer Structures* **14**, 3920 (1996).

[50] Sánchez, E. J. *et al.* Ion and electron beam assisted growth of nanometric Si_mO_n structures for near-field microscopy. *Review of Scientific Instruments* **73**, 3901 (2002).

[51] Hoyle, P. C. *et al.* Electrical resistance of electron beam induced deposits from tungsten hexacarbonyl. *Applied Physics Letters* **62**, 3043–3045 (1993).

[52] Hiroshima, H. *et al.* Fabrication of conductive wires by electron-beam-induced deposition. *Nanotechnology* **9**, 108–112 (1998).

[53] Utke, I. *et al.* Electron beam induced deposition of metallic tips and wires for microelectronics applications. *Microelectronic Engineering* **53**, 261–264 (2000).

[54] Koops, H. W. P. *et al.* Constructive three-dimensional lithography with electron-beam induced deposition for quantum effect devices. *Journal of Vacuum Science & Technology B: Microelectronics and Nanometer Structures* **11**, 2386 (1993).

[55] Mølhave, K. *et al.* Constructing, connecting and soldering nanostructures by environmental electron beam deposition. *Nanotechnology* **15**, 1047–1053 (2004).

[56] Okada, S. *et al.* Growth manner and mechanical characteristics of amorphous carbon nanopillar grown by electron-beam-induced chemical vapor deposition. *Japanese Journal of Applied Physics, Part 1: Regular Papers and Short Notes and Review Papers* **44**, 5646–5650 (2005).

[57] Bret, T. *et al.* Periodic structure formation by focused electron-beam-induced deposition. *Journal of Vacuum Science & Technology B: Microelectronics and Nanometer Structures* **22**, 2504 (2004).

[58] Bret, T. *et al.* Influence of the beam scan direction during focused electron beam induced deposition of 3D nanostructures. *Microelectronic Engineering* **78-79**, 307–313 (2005).

[59] Ding, W. *et al.* Mechanics of hydrogenated amorphous carbon deposits from electron-beam-induced deposition of a paraffin precursor. *Journal of Applied Physics* **98** (2005).

[60] Li, W. *et al.* Study of temperature influence on electron beam induced deposition. *Journal of Vacuum Science & Technology A: Vacuum, Surfaces, and Films* **24**, 431–436 (2006).

[61] Folch, A. *et al.* High-vacuum versus "environmental" electron beam deposition. *Journal of Vacuum Science & Technology B: Microelectronics and Nanometer Structures* **14**, 2609 (1996).

[62] Bret, T. *et al.* (submitted). *Microelectron. Eng.* **83**, 1482 (2006).

[63] Utke, I. *et al.* Density determination of focused-electron-beam-induced deposits with simple cantilever-based method. *Applied Physics Letters* **88**, 1–3 (2006).

[64] Bret, T. *PHYSICO-CHEMICAL STUDY OF THE FOCUSED ELECTRON BEAM INDUCED DEPOSITION PROCESS*. Ph.D. thesis (2005).

[65] Fowlkes, J. D. *et al.* Simulation-Guided 3D Nanomanufacturing via Focused Electron Beam Induced Deposition. *ACS Nano* **10**, 6163–6172 (2016).

[66] Joy, D. C. An Introduction to Monte-Carlo Simulations. *Scanning Microscopy* **5**, 329–337 (1991).

[67] Lau, Y. M. *et al.* Properties and applications of cobalt-based material produced by electron-beam-induced deposition. *Journal of Vacuum Science & Technology A: Vacuum, Surfaces, and Films* **20**, 1295–1302 (2002).

[68] Porrati, F. *et al.* Crystalline Niobium Carbide Superconducting Nanowires Prepared by Focused Ion Beam Direct Writing. *ACS Nano* **13**, 6287–6296 (2019).

[69] Sun, Y. *et al.* Voltage-current properties of superconducting amorphous tungsten nanostrips. *Scientific Reports* **3** (2013).